Celldetective: an AI-enhanced image analysis tool for unraveling dynamic cell interactions

Rémy Torro[1,2*], Beatriz Díaz-Bello[1], Dalia El Arawi[1], Ksenija Dervanova[1], Lorna Ammer[1,3], Florian Dupuy[1], Patrick Chames[3], Kheya Sengupta[2], Laurent Limozin[1*]

[1]Aix-Marseille Univ, CNRS, INSERM, Turing Centre for Living systems, LAI, Marseille, France.
[2]Aix-Marseille Univ, CNRS, Turing Centre for Living systems, CINAM, Marseille, France.
[3]Aix-Marseille Univ, CNRS, INSERM, Institut Paoli-Calmettes, CRCM, Marseille, France.

*Corresponding author(s). E-mail(s): remy.torro@inserm.fr; laurent.limozin@inserm.fr;

Abstract

A current challenge in bioimaging for immunology and immunotherapy research lies in analyzing multimodal and multidimensional data that capture dynamic interactions between diverse cell populations. Here, we introduce Celldetective, an open-source Python-based solution designed for high-performance, end-to-end analysis of image-based *in vitro* immune and immunotherapy assays. Purpose-built for multicondition, 2D multichannel time-lapse microscopy of mixed cell populations, Celldetective is optimized for the needs of immunology assays. The software seamlessly integrates AI-based segmentation, Bayesian tracking,and automated single-cell event detection, all within an intuitive graphical interface that supports interactive visualization, annotation, and training capabilities. We demonstrate its utility with original data on immune effector cell interactions with an activating surface, mediated by bispecific antibodies, and further showcase its potential for analyzing extensive sets of pairwise interactions in antibody-dependent cell cytotoxicity events.

Keywords: bioimage analysis, multimodal microscopy, artificial intelligence, immune cell interactions

Introduction

An overarching goal of post-genomic biomedical research is to decipher cell states and transitions as well as cell interactions in functional dynamic assays [1]. This requires high throughput and high resolution experimental methods supported by advanced and powerful analysis [2, 3]. The field of immunology presents specific challenges, related to complex cell states characterized by transient and heterogeneous receptor expression, highly motile behaviour and immune function relying on dynamic cell-cell interactions [4, 5]. These features are largely out of reach in ensemble biochemical measurements [6] as well as low time-resolution single cell multi-omic data [7].

Microscopy-based *in-vitro* assays can bridge temporal and spatial scales, contributing to decipher lymphocyte activation from molecular to cellular scales [8–10]. Combining high content and high spatial resolution, imaging flow cytometry was applied to reconstruct disease progression on single immune cell populations [11] or to functionally characterize therapeutic antibodies against liquid tumours [12]. The anlysis is however limited to single cell or cell doublets. Multichannel fluorescence microscopy was successfully applied to image-based profiling of human T lymphocytes and Natural Killer cells (NK) [13] or therapeutic targets in drug discovery [14], but it provided limited dynamic information on the system. In certain cases, nanowell grids were used to organize cell-contacts and facilitate image analysis [15, 16] at the expense of imposing less physiological conditions.

High content, multi-channel spatio-temporal imaging of living cells provides rich dynamic and multiscale information across scales, from molecular to cell population [17]. In single-cell image sequences, time-dependent signals contain functional information, traditionally collected or treated manually in immunological settings [18]. Recent methods perform profiling on time dependent data for cellular phenotyping, but without measuring single events in time [19]. Functional dynamic information like calcium imaging can also be extracted for immune cell classification [20, 21] or the activity of neural network in the brain [22]. Most recent works on cell dynamics, specially in the context of cancer immunotherapy, involve specialized microscopy techniques and complex analysis protocoles [23–25], sometimes using proprietary software [26, 27].

In the last years, machine learning and deep learning (DL) have revolutionized the field of image analysis [11, 12, 28–32]. A critical step in the context of cell images is segmentation, for which DL tools are highly successful [33–38]. However, they often rely on pretrained models for which the original dataset is not always accessible or too remote from users' data [39], limiting the adaptability. For dynamic data, the tracking of cells is also crucial and can be performed by available tools [40–42]. Recent methods that integrate profiling with time-dependent information significantly enhance cell tracking performance [43–45]. However, current software associating the two tasks are mostly applied to the analysis of cell lineage [41, 46–48]. Most popular generalist and free software like Fiji [49], Icy [50] or Cellprofiler [51] either don't offer intrisic DL methods or only via derivatives [52], or are not conceived for time-dependent data

[53]. Finally, end-to-end analysis tools accessible to experimentalists, adapted for both image and time-signal are currently lacking, preventing data curation and DL based event-detection. With the exception of MIA [54], existing partial solutions require coding skills [55] or proficiency in integrating/mastering disparate tools [56].

We introduce Celldetective, an open-source software designed to tackle the challenges of analyzing image-based *in vitro* immune and immunotherapy assays. It addresses the problem of cell interactions by extracting and interpreting single-cell behaviors for up to two populations of interest in a 2D co-culture, with a cell pair description linking the populations. The software adapts to varying imaging conditions and cell types, incorporating dataset curation and Deep-learning model training features directly within the graphical user interface (GUI). Celldetective organizes and automates complicated, time-consuming processes while providing a user-friendly, no-code GUI, making it accessible to experimental scientists without programming expertise. We tested the software on two applications in immunology and immunotherapy: i) measuring immune cell behavior in contact with an antigen-presenting surface using a label-free microscopy technique, and ii) assessing dynamic cell-cell interactions in a multiwell co-culture of immune and target cells, an established cytotoxic assay, using multicolor fluorescence microscopy.

Results

Software analysis pipeline

Celldetective is implemented as a Python package with a PyQt5-based GUI, available through the PyPi package repository and regularly updated. The source code can be accessed on GitHub (https://github.com/celldetective/celldetective), while all models, datasets, and demos are hosted in a public Zenodo repository (https://zenodo.org/records/13907294). Extensive documentation is hosted on Read the Docs (https://celldetective.readthedocs.io). The software is designed to run locally on a single computer equipped with either a graphics processing unit (GPU) or multiple processors. Image processing is conducted frame by frame with garbage collection to significantly reduce memory requirements, allowing it to operate on most laboratory computers. Celldetective is compatible with multi-channel time-lapse microscopy image stack files in TIF format, which are typically generated by acquisition software such as Micro-Manager [57].

As illustrated in Fig. 1, the software input consists of an experimental project that organizes raw data into a two-level folder structure emulating a multiwell plate, commonly used in *in vitro* immune assays (see the project startup window in Fig. S6A). At the top level, folders represent each well (or biological condition), while the second level contains folders for each position (a field of view associated with the biological condition). Experiment metadata – including channel names and order, spatiotemporal calibration, and biological condition labels – are stored in a configuration file created during project setup (project creation window shown in Fig. S6B). Users manually deposit each image stack into the respective position folder. This project structure organizes the experimental data by biological conditions and field of views, facilitating sequential processing of all conditions.

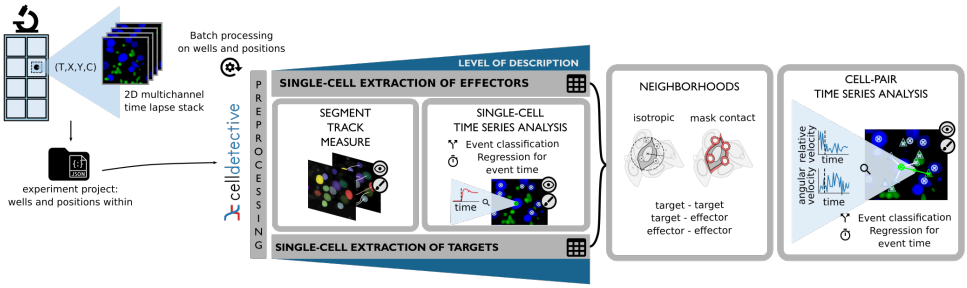

Fig. 1 Software Overview: An end-to-end GUI pipeline for studying interactions between target and effector cell pairs (from left to right). After loading an experiment project that mimics a multiwell plate structure, including wells and positions within wells, the user can apply preprocessing steps to the 2D time lapse microscopy images before segmentation. Target and effector cells are then segmented, tracked, and measured independently. Events are detected from the resulting time series, and the co-culture images are distilled into tables of single-cell measurements. The neighborhood module links cells in spatial proximity, and the cell-pair signal analysis framework facilitates the investigation of interactions between cell pairs. Eye and brush icons indicate steps where visual control and corrections are possible, with an appropriate viewer.
Fig. S6. Main GUI windows.
Fig. S7. Processing modules to extract single cells.
Fig. S8. Background correction methods.
Fig. S9. Overview of segmentation strategies.
Fig. S10. Event detection model architectures.
Tab. S2. Generalist Deep-learning segmentation models.

Upon loading a project, a modular interface organizes all possible user actions (Fig. S6C with functionalities to extract single cells illustrated in Fig. S7). The first module, dedicated to image **preprocessing**, enables users to transform images prior to segmentation. Two independent processing modules facilitate single-cell analysis: one for effectors and the other for targets. Population-specific **segmentation**, followed by optional **tracking** and **measurements**, reduces the image stacks into tables, with each row representing a single cell at a specific time point. When tracking information is available, single-cell measurements are structured as time series, which are then analyzed to detect **events**. Alternatively, users can **classify** cells at each time point based on measurements using a dedicated module. A viewer submodule is integrated at each step for quality control, error correction, or data annotation. The final module addresses cell **interactions** within or across populations, enabling users to describe, interpret, and annotate cell pairs. Throughout the process, users can plot and compare measurement distributions of individual cells or cell pairs via a table exploration module designed for manipulating cell tracks. Additional analysis tools allow for the representation of survival curves and synchronized time series.

Preprocessing: Image preprocessing can facilitate segmentation and data interpretation. To this end, we implemented two easy-to-configure background correction techniques (illustrated in Fig. S8). Both methods rely on cell exclusion achieved by setting a threshold on the standard deviation-filtered image. This process is facilitated by an intuitive viewer and a slider that visually indicates the cell selection

for each threshold value. The fit-based method estimates the background for each image by fitting a model (either a paraboloid or a plane) to the non-cell pixels. In contrast, the model-free method stacks the background estimates from all positions and performs a median projection to derive a single background estimate per well. The background is then applied to the images through subtraction (for fluorescence images) or division (for brightfield and reflection images), with optional clipping. This preprocessing can be performed sequentially on any channel of interest, generating a copy of the original stack for each position.

Segmentation: Celldetective's framework expects the segmentation to be specific to the population of interest (targets or effectors). In co-culture setups, cell populations often overlap spatially in images unless there is ideal channel separation. While it is possible to segment all cells and classify them either simultaneously [58] or in two steps [59], label contamination from overlapping populations remains an issue. Effector cells, for instance, can screen underlying target cells, compromising accurate detection of the latter. We initially applied widely used, open-source Deep-learning segmentation models from StarDist [35] and Cellpose [37], but found limitations due to their lack of specificity. The generalist Cellpose model struggled with mixtures of differently sized cells and rare microscopy modalities (e.g., cell-surface application). Additionally, the two-channel input constraint was problematic, as we often required up to four channels for unambiguous identification of our population of interest (e.g., cell-cell application). Consequently, we trained StarDist and Cellpose models, from scratch and in within the software, to detect a specific cell population, using careful expert annotations and as many channels as necessary (see Applications). Users can utilize generalist StarDist and Cellpose models that work broadly across cell types but lack specificity (Supplementary Tab. S2), our population-specific models tailored to particular applications (tables S3, S4), or train new models on their own data with annotations generated in Celldetective.

Recognizing that traditional segmentation methods can sometimes outperform Deep-learning alternatives due to issues such as annotation bias, training limitations, and inference time, we designed a scheme that integrates both approaches for complementary use (Supplementary Fig. S9). A graphical interface enables the creation of a traditional segmentation pipeline (Supplementary Fig. S11), including image pre-filtering, thresholding, watershed, and feature-based filtering. After segmentation, labels can be opened in napari [56] for manual correction (Supplementary Fig. S12) to address common challenges, such as wrong separation of contiguous cells, false positives, and over-segmentation in crowded regions. We also developed a plugin to export label annotations from image crops, automatically correcting frequent annotation errors. These exported labels, along with the corresponding image and a configuration file, form a ready-to-use sample for training or retraining a Deep-learning segmentation model.

Tracking: Celldetective provides a graphical interface for the open-source Python package bTrack [41], integrating its Bayesian tracker, which, after tuning, proved well-suited for tracking immune and cancer cells in our applications. We developed a configuration interface that enables users to view and adjust the bTrack configuration file (defining the motion model and tracklet reconnection parameters) or to import

configurations from the bTrack-napari plugin. Typical bTrack configuration files are provided for the applications we present. Additionally, users can incorporate mask-based measurements to enhance the Bayesian update, with feature normalization handled automatically by the software. Finally, users can set options for track post-processing (interpolation, extrapolation, filtering) to refine and correct the tracking data. A tracking quality control module visualizes the raw bTrack output (before post-processing) in napari, recoloring labels to preserve cell identity.

Measurements, classification, events: Considering the cellular event variability we were interested in and the drastic information reduction of the microscopy image stacks into tabular data, it seemed crucial to be able to extract as much information as possible about the single cells. We allow users to configure and perform both mask-based measurements (tone, morphology, and texture [60]) and position-based measurements (tone), with integrated viewers that enable parameter tuning directly from images and labels, such as adjusting mask slice measurements, spot detection, and radius for position-based measurements. We also provide on-the-fly background correction procedures (in contrast to the preprocessing module). Alongside the previously mentioned background fit correction, we implemented a local correction method that uses cell masks to estimate and correct for the local background intensity at the cell outer edges. For tracked cells, the measurements are appended to the single-cell tracking table; otherwise, they generate a table without track identities.

We developed a module to classify cells by writing conditions on the measurements with AND and OR logic gates. A flow-cytometry-like scatter plot showing the classification result at each time point for any combination of measurements assists the user in writing arbitrarily complicated conditions. This classification is instantaneous, as each cell from each time point is classified independently. With cell tracks available, we can perform a time-correlated analysis of the binary condition response for each cell. We implemented two particular descriptions: the first is that the cell has a unique state (condition always true or false): the median response determines the cell class; the second is the irreversible event, introduced to describe the cellular events in our applications. It implied three possible states for each cell: always false (no event observed), always true (the event happened before the beginning of observation), or transitioning from false to true (the event occurred during observation). For transitioning events, the software catches the event time by fitting a sigmoid over the binary response for each cell.

To enable single-cell exploration, we implemented an interactive viewer that displays cells directly on microscopy images. Cell mask contours are visible, allowing users to confirm the regions of interest (ROI) used for mask-based measurements, while colored circles mark cell positions. The colors represent cell states for a selected classification or event. By clicking on a cell, users can examine how specific measurements compare across other cells in the image or position. This viewer also allows users to reclassify cells or annotate them with new descriptions as needed.

To facilitate monitoring and annotation of cellular events, we developed an event annotation viewer that loops through the image stack overlaid with cell positions at a high frame rate. This setup, while ideal for visual event detection, has limited time resolution. By selecting a cell within the viewer, users can classify it into one of the

three event classes described earlier, examine the associated time series, and pinpoint the transition time with sub-frame precision (better than half the experimental frame rate). Annotated data from multiple positions can then be exported to form a dataset for the event of interest.

To automate event detection, we implemented a Deep-learning approach with two convolutional models: (1) a classifier that assigns each cell to one of three event classes based on selected measurement time series, and (2) a regressor that estimates the event time for cells exhibiting the event, using the same time series input. Both models share a common backbone, a modified 1D ResNet, designed to process multivariate time series (Supplementary Fig. S10). To match the user-defined input tensor size, time series endpoints are extrapolated by repeating the edge values. In the training set, the time series are augmented with random noise and time shifts to balance the classes and generate artificially a quasi uniform event time distribution. Users can opt to use our pre-trained event-detection models for specific applications (Tab. S5) or easily train new models on their own datasets generated within the associated viewer, with only a few clicks.

Cell interactions: Single cells from two populations can be linked through a neighborhood scheme, which can either define relationships within a single cell population (e.g., targets-targets) or across two distinct populations (e.g., effectors-targets). To accommodate specific application requirements, we developed two distinct neighborhood methods. The mask contact method identifies touching cell masks at any time point, using mask dilation to allow a tolerance for cell contact. The isotropic method, by contrast, disregards cell masks and instead uses a circular region of a selected radius, centered on a reference cell's centroid, to determine neighboring cells. This approach is particularly useful for quantifying cell co-presence in cases with nuclear segmentation or unreliable masks. Neighbor counts extend the single-cell data tables in the same way as other single-cell measurements (more details in Supplementary Fig. S13). The reference-neighbor pairs identified at least once are then measured (e.g., relative distance, angle, velocity) and stored as rows in a cell-pair table. Similar to single cells, these pairs can be classified and annotated through an interactive cell pair viewer, which will be demonstrated in the second application.

General features: The diverse software functionalities are listed and compared to existing software in Table 1. Notably, Celldetective stands out by offering training and transfer options in segmentation, enabling detection of a population of interest within a mixed population, as well as time series annotation and survival analysis, not currently integrated in any other software.

High-throughput analysis of time-resolved cell adhesion and spreading responses

In this first application, we investigated the dynamics of human primary Natural Killer (NK) immune cells as they sedimented and spread on cancer-cell-mimicking surfaces. These assays offer rich spatiotemporal insights into interactions between lymphocytes and surrogate antigen-presenting cells [10, 61, 62]. The bispecific antibody (bsAb) studied here, with potential therapeutic applications, bridges the NK cell's activating receptor CD16 and the surface-bound antigen Human Epidermal Growth Factor

Table 1 Comparative table of software functionalities with a selection of available solutions. A ✓is attributed if the task can be carried without coding. The use of an integrated solution or plugin is indicated in parentheses.

Software feature	ImageJ/Fiji	CellProfiler	CellACDC	MIA	Celldetective
Ref.	[49]	[51]	[47]	[54]	this work
Traditional segmentation	✓	✓	✓	✗	✓
DL segmentation	✓	✓	✓	✓	✓
Corrections annotations	✓ (Labkit)	✓ (GIMP)	✓	✓	✓ (napari)
Training	✗	✗	✗	✓	✓
Transfer	✗	✗	✗	✓	✓
Tracking	✓ (TrackMate)	✓ (TrackObjects)	✓	✓ (Hungarian)	✓ (bTrack)
Visualization	✓ (TrackMate)	✗	✓	✓	✓ (napari)
Position-based measurements	✓	✗	✗	✗	✓
Measurement classification	✗	✓	✗	✗	✓
Signal annotations	✗	✗	(✓) cell-cycle	✗	✓
Interaction analysis	✗	✓	✗	✗	✓
Experiment manager	✗	✗	✓	✗	✓
Multi-condition data exploration	✗	✓ (CP Analyst)	✗	✗	✓
Survival analysis	✗	✗	✗	✗	✓

Receptor 2 (HER-2), a breast cancer marker. Our objective was to evaluate the bsAb's effectiveness in promoting cell spreading, used here as a proxy for antibody-mediated cell-cell interaction [61, 63]. We imaged cell behavior at the surface interface using reflection interference contrast microscopy (RICM), a label-free technique sensitive to submicrometer distances between the cell membrane and the surface [64] (Fig. 2A).

Cell segmentation in RICM images is challenging because the cells can be locally brighter and darker than the background, causing direct thresholding techniques to fail [64]. To address this, previous approaches have adopted special techniques, such as background correction and applying a variance filter before thresholding [10, 65, 66]. Here, we focused on segmenting lymphocytes that were spreading or hovering on the surfaces. Following background correction using the model-free technique described earlier, we designed a traditional segmentation pipeline within Celldetective (Supplementary Fig. S11). An expert then manually corrected labeling errors in the label viewer module (napari, Supplementary Fig. S12), using cropped

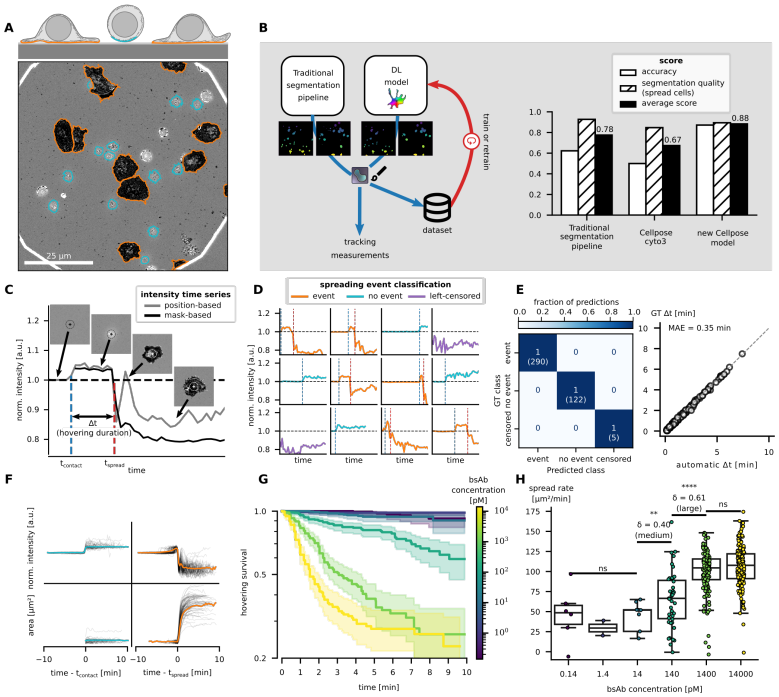

Fig. 2 Functional response of immune cells in a spreading assay. A) Schematic (top) and snapshot (bottom) of a spreading assay imaged by time-lapse RICM. Primary NK cells sediment on an HER2 coated surface in the presence of bispecific anti-CD16 × HER2 antibodies. Cells touch the surface in a desynchronized manner and may spread after a stochastic hovering duration. The contours of the cells are represented in orange for cells classified as spread on the surface and blue for hovering cells (corresponding colors are also used in the schematic). B) A traditional segmentation pipeline is used to generate a first instance segmentation of the cells imaged in RICM. Cell masks can be manually curated before training a new Cellpose [36] model starting from scratch or from an existing generalist model. Barplot comparing segmentation scores obtained for three different methods that can be called within the software. With the improved results yielded by the new model, the user can proceed to tracking and measurements. C) Intensity time series for a cell performing a contact and spreading sequence (see text for details). D) Single-cell intensity time series color-coded for three classes: 1) the cell spreads during the movie ('event', orange), 2) the cell is not observed to spread during the movie ('no-event', green) and 3) the cell is already spread at the beginning of the movie ('left-censored', purple). E) Benchmarking of cell class automatic determination reported by a confusion matrix, and comparison of spreading times determined automatically. F) Individual cell time series (tonal, morphological, etc) are synchronized with respect to a characteristic time to measure the average population response at the event time. G,H) Functional response for the cell population as a function of bsAb concentration: hovering survival or distribution of cell decision time before spreading (G), spreading rate (H).
Fig. S11. Designing a traditional segmentation pipeline.
Fig. S12. Segmentation correction and annotation.
Video: ricm_events.mp4

regions from multiple biological conditions to separate contiguous cells, remove false positives (e.g., red blood cells), and add missed detections. Figure 2A shows an

example of expert annotation, where the contours of spread cells appear in orange and those of hovering cells in cyan, while red blood cells and surface defects visible in the image are excluded. With Celldetective, the expert could generate a large dataset of labeled lymphocytes imaged in RICM within minutes per image.

Our goal with this dataset was to train a DL model to eliminate the need for expert corrections. The complete strategy – generating an initial set of labels with the traditional segmentation pipeline, correcting errors in the viewer to build a training dataset, and training a DL model from this dataset – is illustrated in Figure 2B. Using this approach, we trained a new Cellpose model on the dataset to selectively segment lymphocytes from RICM images (both the dataset and model are available on Zenodo). We benchmarked this model against the traditional segmentation pipeline and the cyto3 generalist Cellpose model [37] using a test set, quantifying lymphocyte detection accuracy and segmentation quality for spread cells separately (see Materials and Methods for details). Hovering cells, which appeared as bright blobs with interference patterns and had an ill-defined area in RICM, were excluded from the segmentation quality score. In Fig 2B, we show the scores achieved by the three methods on the test set, decomposing detection accuracy and segmentation quality from the average score. Our newly trained model achieved a higher detection accuracy of 0.86, compared to 0.62 for the traditional pipeline and 0.5 for the generalist model. The traditional pipeline tended to produce many false-positive detections, while the generalist model struggled to simultaneously detect spread and hovering cells. Segmentation quality, however, was higher for the pipeline (0.93) than for our model (0.89) or the generalist model (0.88). Since most spread cell labels in the test set required little manual correction (except for contiguous cells), it was unsurprising to observe the highest segmentation quality for the pipeline method. The generalist model segmented spread cells well when it could detect them. Overall, the new Cellpose model achieved the best average performance across both tasks (0.88), making it the most effective approach for segmenting cells in this assay.

With accurate cell masks generated, the next step was to track the cells. Cells demonstrated rapid motility in their hovering state and quasi-stationary motion in their spread state. Tracking was performed using a versatile motion model (see Materials and Methods), without feature inputs to prevent sharp morpho-tonal transitions from disrupting tracking accuracy. We enabled track extrapolation from the beginning of the movies, allowing intensity measurements to start before the cells reached the surface. The resulting intensity time series for an example track is shown in Figure 2C-D. With track post-processing, we could measure intensities prior to cell arrival using the previously described position-based measurement, which compared well with the mask-based measurement. Notably, the position-based intensity showed a spike during the spreading phase, which was not observed in the mask-based intensity.

In these experiments, cells sedimented under gravity, becoming visible in RICM when they were within a few hundred nanometers of the surface [64]. The cells could scan the surface, before engaging in spreading, characterized by a contrasted footprint on the image [61]. We sought to define characteristic events to describe the cells behavior. By examining the images and RICM intensity time series, we identified two such events (Fig. 2C). We defined the contact time (t_{contact}) as the moment when

the cell first appeared in RICM, with an average intensity greater than 1 (indicated by the blue dotted vertical line). The onset of spreading (t_{spread}) was marked by the point at which the average intensity dropped below 1 (red dotted vertical line). The difference between these two times defined the hovering time, which, for spreading cells, corresponded to the time required to make a spreading decision.

Based on this event description, we sought to automate event detection. The contact time for a given cell corresponded to the time of its first segmentation, an event automatically detected by the software. Spreading events were identified through condition-based classification (mask-based RICM intensity < 1) and an irreversible event hypothesis, as described earlier. We benchmarked classification performance and hovering duration estimates against a manually annotated test set. Fig. 2D presents the intensity time series of several cells, color-coded by their automatically assigned class and estimated event time (when applicable) with respect to spreading events. A confusion matrix indicates perfect agreement between automatic classification and ground truth, while a correlation plot comparing estimated hovering durations to the ground truth shows excellent agreement, with a mean absolute error of 0.35 minute (Fig. 2E). In practice, we performed quality checks on the detected events using the event annotation viewer described in the previous section (Video ricm_events.mp4).

After automatically extracting the event times, we examined whether an average population response could be reconstructed from single-cell time series. Using the software, we synchronized each single-cell measurement to a specific event time and calculated the mean response across the population. Figure 2F shows the mean population response for the mask-based area and RICM intensity measurements, decomposed by the spreading event class within a single biological condition. On the left side (cyan), cells not exhibiting a spreading event are synchronized to t_{contact}. On the right side (orange), spreading cells are synchronized to t_{spread}. Single-cell time series are represented in black. This alignment of single-cell time series, with low lateral variance near event times, supports the hypothesis of an irreversible event and confirms the detection quality for this system. The gradual increase in RICM signal observed before t_{spread} for spreading cells did not appear in isolated single-cell time series. This artifact results from asynchrony in the time series relative to the contact time, underscoring the importance of both event times for characterizing the system and highlighting the need to focus on the hovering duration.

With a clear definition for the spreading event and decision time, we tested whether the probability to observe a spreading event was modulated by the surface condition. We estimated the survival of the cells in the hovering state, synchronized to the contact time with Celldetective. The survival curves, decomposed by bsAb concentrations (Figure 2G), show an increase of the fraction of cells exhibiting a spreading event (endpoint fraction) and faster spreading decision times with increasing bsAb concentrations. The acceleration of the spreading decision time was particularly apparent in the 10-1000 pM bsAb concentration range, saturating beyond 100 pM.

After demonstrating that cells took less time to initiate spreading with increasing bsAb concentration, we next examined whether they also spread at a faster rate. Using the table exploration feature in Celldetective, we differentiated the area with respect to time for each cell track, extracting the spreading rate at the onset of spreading

(t_{spread}). This rate, shown in Figure 2H across increasing bsAb concentrations, reveals a significant increase with moderate to large effect sizes in the 14-1400 pM range.

Overall, determining the spreading decision time for individual cells to spread, measured at high throughput, highlights Celldetective capabilities in exploring immune cell-surface interactions.

Cytotoxic response in a co-culture with overlapping channels

In the second application, we studied antibody-dependent cell cytotoxicity (ADCC) in a high-density co-culture of target tumor cells (MCF-7) and effector cells (primary NK) for various biological conditions (concentration of bsAb anti-CD16 $\times$ HER2, tumor cell HER2 expression). Dyes were introduced just before the observation to label the cell nuclei with Hoechst (blue), NK cytoplasm with CFSE (green), and the nuclei of dead cells labeled with propidium iodide (PI, red). After effector cell introduction, the system was imaged in multichannel (brightfield and the three epifluorescence channels) time-lapse for 2-3 hours for up to 8 biological conditions simultaneously. A multi-color composite representation of a single position is shown at endpoints in Figure 3A, illustrating how the number of dead (red) nuclei increases over time.

First, we studied the lysis behavior of target cells over time, which entailed achieving a single-cell description for the target cells. MCF-7 cells are notoriously challenging to segment from the brightfield channel [39]. As a result, we focused on segmenting solely their nuclei. As illustrated in Figure 3B, while MCF-7 nuclei were easily visible at the beginning of the movies, the effectors took the Hoechst dye over time, and the MCF-7 nuclei tended to lose their signal and become blurry upon death, making their segmentation harder as time progresses.

Initially, we tried to segment the nuclei using generalist nuclear segmentation models (StarDist *versatile fluorescence* and Cellpose *nuclei* models) on the Hoechst channel. We achieved poor accuracy performances due to the low specificity of these models and moderate segmentation quality, limited by eclipsing effects (see fig Supp MCF7 benchmark). As before, we had an expert annotate specifically MCF-7 nuclei, using all available multi-channel and time information, in these co-culture images for several biological conditions and experiments (dataset provided in Zenodo). Since the MCF-7 and primary NK cell nuclei are morphologically different, we expected to be able to train an efficient model detecting the MCF-7 nuclei from the Hoechst channel only, failing only on blurry images, where the morphological separation is no longer obvious. We used Celldetective to retrain StarDist *versatile fluorescence* model on our dataset using the Hoechst channel as its input and considerably improved the performance, increasing from 0.55 to 0.82. Last, we trained a completely multi-channel model on all four available channels to detect the MCF-7 nuclei and achieve a slightly higher performance (0.83). All of the models benchmarked are accessible directly in Celldetective (see Supplementary Tab. S2 and S3).

The MCF-7 nuclei were tracked with a quasi-stationary motion model, allowing for small displacements and potentially long-time gaps. We passed the Hoechst and PI intensities and the nuclear apparent area to the tracker which helped in experiments where the live/dead transitions were not too sudden. Cells not present in the first frame of the movie were filtered out to limit the number of false positive detections

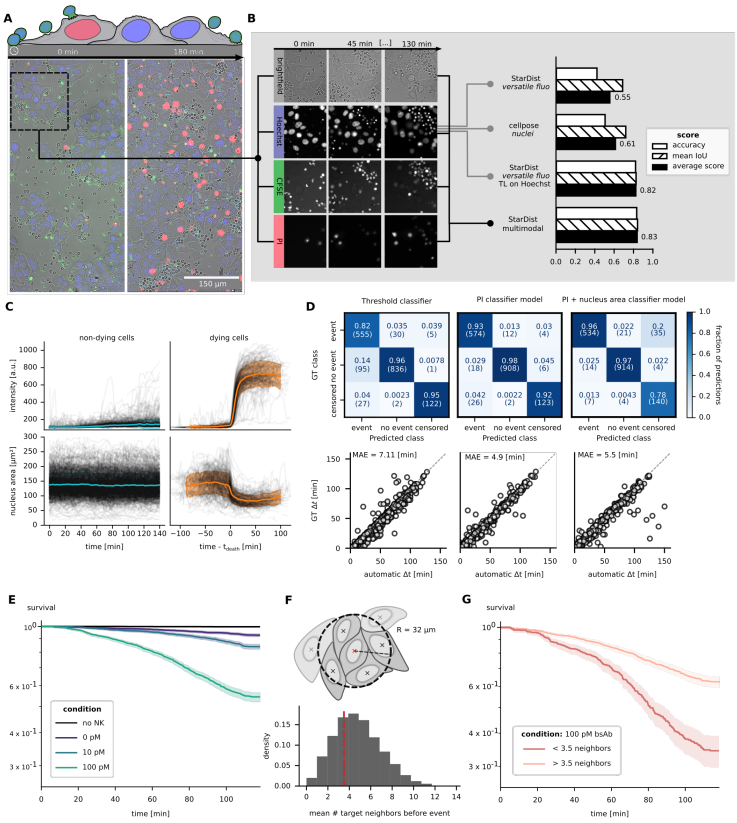

Fig. 3 High throughput cytotoxic response of cancer cells in co-culture with immune cells. A. Schematics side-view of target/NK cells co-culture assay for bispecific ADCC (top) and representative multimodal composite images, obtained at two different time points, with target nuclei labelled in blue, dying cells in red and NK cells in green (bottom). Corresponding colors are also used in the schematics. B. Decomposition of partly overlapping fluorescence channels and benchmark of segmentation DL models. Brightfield and fluorescence images at three different time points. Hoechst channel (target nucleus) is taken as input for existing StarDist versatile fluo or cellpose nuclei models (available directly from celldetective). Two new models trained within celldetective were benchmarked: transfered learning based versatile fluo model, Hoechst as input. StarDist multimodal is trained from scratch using 4 channels as input. C. Time traces of nuclear fluorescence intensity and nucleus apparent area for a set of non-dying target cells (left) and of dying cells (right); the reference time t_0 is the death time for the dying cells. D. Benchmark of three methods for event classification and regression (Threshold method on PI, DL classifier on PI, DL classifier on PI and nucleus area). Top row: confusion matrices with 3 classes. Bottom row: correlation plots. E. Survival curves of target cells without NK cells or in the presence of NK cells for different bsAb concentrations. F. Schematics for neighbors counting and histogram of target neighbors count. G. Survival curves for two subpopulations of targets at 100 pM bsAb, splitted as a function of the local target cell density. Tab. S3. MCF7 nuclei segmentation models.
Tab. S5. Event detection models.
Video: adcc_rgb.mp4

and exclude daughter cells from our study. Tracks were extrapolated until the end of

the observation to measure intensities at the last detected position, which worked well in this system since the nuclei were mostly stationary.

In this experimental design, dying tumor cells are expected to turn red (Figure 3A), visible in the PI intensity time series generated for each cell track. To characterize tumor cell death events, an expert reviewed the images and PI intensity time series, annotating death events defined by a sharp increase in PI signal at t_{death}. Single-cell time series were then grouped by event class and synchronized to t_{death} (Figure 3C). The average PI intensity for cells undergoing death shows a distinctive step-like transition with low lateral variance, validating the annotation accuracy (Fig 3C, top-right). The PI signal in live cells, by contrast, rises slightly over time but remains well below the levels observed in dead cells (Fig 3C, top-left). Notably, the apparent nuclear area of dying cells contracts sharply at t_{death} (Fig 3C, bottom-right), while the nuclear area of non-dying cells remains constant (Fig 3C, bottom-left).

To detect death events for between 400 and 1,500 tumor cells per position, we evaluated the most effective event detection method available in our software. An expert annotated a test set from movies previously unseen by our event detection models. We then assessed the performance of three methods on this dataset: (1) a condition-based classification using the irreversible event hypothesis on the PI intensity time series, (2) a DL model trained to detect death events from PI alone, and (3) a DL model trained to detect events using both the PI intensity and nuclear area time series. Detailed information on the training procedures for these models is provided in the Materials and Methods section. Figure 3D presents the confusion matrices for each method, showing agreement between predicted and ground-truth event classes, along with a correlation plot evaluating the accuracy of death time extraction. The condition-based classification method, although effective at identifying cells already dead at the beginning of the observation, incorrectly predicted about 15 % of the events as death events when none had occurred. This method also had the highest mean absolute error (MAE) for death time estimates (7.1 minutes), partly due to its systematic bias in detecting the center of the step function rather than the onset of PI increase. The PI-only event detection model performed better, with only 3 % of its predicted death events corresponding to an absence of events. The multivariate model, incorporating both PI and nuclear area data, achieved the highest precision in death event detection (96 % of predicted death events were true events). However, this model showed a reduced accuracy in identifying cells as already dead, with 20 % of these cells (2 % of the total number of cells) observed to die later. The PI-only model yielded the most accurate death time estimates, with an MAE of 4.9 minutes (to relate to typical frame rate of 2-5 minutes). As before, and in practice, quality check and minor manual corrections were performed with the event annotation viewer, using this time a multichannel composite of the images (Video adcc_rgb.mp4).

After identifying lysis event times – marked by an increase in PI signal within the nucleus and a reduction in apparent nuclear area – we investigated whether the probability of tumor cell lysis depended on bsAb concentration. We assumed that all tumor cells experienced the same lysis risk upon NK cell introduction, which occurred a few minutes before observation began. Using t=0 min as the synchronization time, we excluded cells already dead at the start (always less than 5%) and disregarded

cells born from mitosis (during tracking post-processing). We represented the MCF-7 survival curve using t_{death} as the event time (Figure 3E), which shows an increase in the fraction of dead MCF-7 cells (endpoint fraction) occurring at a faster rate with rising bsAb concentrations.

While cell lysis could also be analyzed without single-cell resolution or without imaging entirely, these approaches risk interference from PI signals generated by dying NK cells. Here, our objective was to leverage a single-cell approach to link cell survival with local context. To do this, we calculated a target-target neighborhood within a 32 μm radius, using the time-averaged neighbor count up until the lysis event as an indicator of the local density experienced by each target cell until death. Figure 3F shows the distribution of this measure. We then applied a filter in Celldetective to compare survival outcomes for cells in low-density versus high-density environments (Fig 3G), observing a significant survival advantage for targets in high-density regions.

From a single time point to a dynamic readout of effector-target interactions

After describing the ADCC assay from the target cells perspective, we shifted our focus to effectors. Single NK cells were segmented using a custom multichannel Cellpose model that combines Brightfield, Hoechst, and CFSE, a cytoplasmic fluorescence label (see Supplementary Tab. S4). This model is sensitive to cells both out of plane (high contrast in Brightfield but faint and blurry in CFSE) and in synapse (nearly invisible in Brightfield). Unlike targets, the effector cells exhibit high motility and can form dense clusters in the assay, both of which limit reliable tracking. Consequently, the software offers two levels of analysis, depending on cell track availability.

When effector tracking was unfeasible (e.g., at an effector-to-target ratio of 5:1 and inter-frame time greater than 2 minutes), we could still analyze the cells at each time point to compare biological conditions. We aimed to measure the signal from fluorescently labeled antibodies, each tagged with a single ATTO 647 dye. Specifically, we compared the CE4-21 bispecific antibody with the CE4-X control antibody, which binds only to the HER2 antigen on target cells, across two target cell lines with distinct antigen expression levels (WT and HER2+) [67]. The mean bsAb fluorescence intensity over each NK cell mask was measured following an on-the-fly background correction of the raw images. Target cell contact with NK cells was inferred using a radial neighborhood calculation, as only target cell nuclei masks were available, and was further classified by the number of neighboring target cells: an NK cell in contact was defined as having at least one target neighbor (inclusive counting convention, see Supplementary Fig. S13). A quality check of this contact classification was performed in-situ on the images using a dedicated viewer (Video single-timepoint-contact.mp4). Figure 4 presents the mean fluorescence intensity of effector cells at a selected time point (1 hour), broken down by target cell type, antibody type, and contact class. For WT targets (lowest HER2 expression), effector cells displayed fluorescence in the CE4-21 bsAb condition, regardless of contact status with the target cell (Figure 4A). In contrast, the CE4-X antibody condition showed no signal, supporting that the detected fluorescence signal originated exclusively from effector cells, as can also be seen visually in Figure 4B.

Using CE4-21 bsAb measurements, we investigated whether the fraction of fluorescent-positive effector cells was associated with their contact status relative to wildtype target cells. Cells with a mean fluorescence intensity above 50 a.u. were classified as fluorescent-positive, and the proportions of these cells in contact versus off-contact with target cells are displayed in the inset of Fig. 4A. Results indicate a significantly higher fraction of fluorescent-positive effector cells off contact compared to those in contact, with a small effect size (Cliff's Delta > 0.147). With the HER2+ target cells and CE4-X antibody condition, the signal measured off-contact from the target cells was negligible, confirming that the antibody did not bind to the effector cells (Fig 4A-B). The signal captured in contact did not originate from the effector cells but from what was below, i.e. the target cells. With the CE4-21 bsAb, on the other hand, the signal measured in contact was a sum of contributions from both the target and effector cells. Off-contact, we had an estimate of the effector cells' contribution.

Based on the measured signals, we sought to determine whether the combined effector signal from the CE4-21 bsAb in the off-contact condition (without target contribution) and the effector signal from the CE4-X antibody in the in-contact condition (without effector contribution) could approximate the signal observed in the CE4-21 in-contact condition. Using the distributions generated by the software, we performed a Monte Carlo simulation to create a distribution of this summed signal and compared it with the CE4-21 in-contact condition. The empirical cumulative distribution functions (ECDFs) for the simulated (gray) and observed (orange) distributions are shown in Figure 4C, with the KS statistic (the maximum distance between the two ECDFs) indicated by a dotted black line. Our results reveal that the simulated signal distribution was significantly lower than that of the CE4-21 in-contact condition, with a small effect size (Cliff's Delta > 0.33). By calculating this effect size at each time point, we further confirmed the robustness of this finding, as the effect consistently maintained the same direction, with a medium effect size observed more often than not (Suppl. Fig. S14).

If effector tracking is achievable (an effector-to-target ratio of 1:1 and a time between frames lower than 2 minutes), we can explore the measurement time series or extract time-averaged estimators, as with the target cells. We illustrate this software feature by adding a degranulation marker (fluorescent anti-LAMP1) to monitor the lytic activity of the effector cells in the ADCC assay. In this experiment, we compared two bsAbs, CE4-21 and CE4-28, formed of the same CE4 nanobody against HER2 and two different nanobodies against CD16 on the effector side.

First, we investigated whether LAMP1 expression was influenced by biological conditions, mirroring our approach with fluorescent antibodies. The software was utilized to measure the mean LAMP1 intensity over each NK cell mask following background correction of the raw images (see Materials and Methods for details). We classified cells as LAMP1-positive or LAMP1-negative at each time point using an intensity threshold ($I_{\mathrm{LAMP1}} > 5$ a.u.). For each target cell type and antibody condition (no antibody, CE4-28 bsAb, CE4-21 bsAb), we reported the fraction of LAMP1-positive effector cells both in contact with and off contact from target cells across all time points (Fig. 5A). The results indicated that, except for the controls

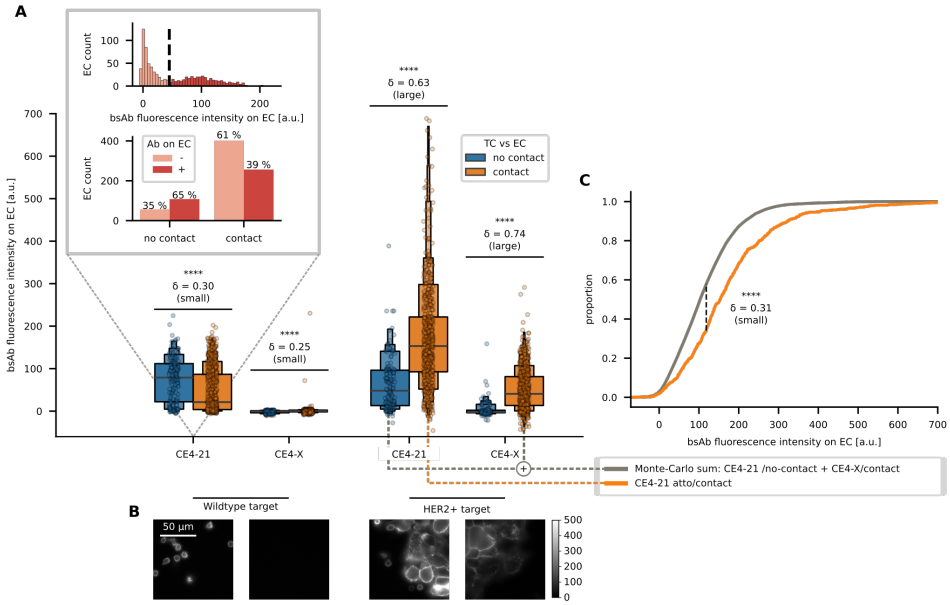

Fig. 4 Single time point analysis of effector-target interactions. In the absence of effector tracking, fluorescent bsAbs were used to study the distribution of Ab on effectors and targets. A. bsAb intensity measured on effector cells on targets with high or low antigen expression. bsAb CE4-21 binds to both HER2 and CD16, while CE4-X control antibody binds only to the HER2 antigen on target cells. Inset: Exploration of condition CE4-21 on WT target. Intensity histogram to classify bsAb positive and negative cells. Count of bsAb positive and negative cell in contact or no contact with target cells. B. Representative snapshot of fluorescence channel for each condition of A. C. Cumulated distribution of fluorescence intensity, comparing CE4-21 contact case and the sum of CE4-21/no contact + CE4-X/contact.
Fig. S13. Proposed neighborhood counting methods.
Fig. S14. Running statistics for comparing Abs fluorescence level.
Tab. S4. Primary NK segmentation models.
Video: single-timepoint-contact.mp4

without antibody, the fraction of LAMP1-positive cells was consistently higher when in contact with target cells.

From this time-integrated approach, we shifted our focus to the dynamics of the effector cells, specifically investigating whether their motility was influenced by target cell proximity. Given that velocity estimators can be noisy, we computed a time-averaged velocity estimate for each cell track, similar to the target density estimates for target cells. Additionally, we utilized our contact classification to extract velocities separately for each cell state (in contact vs. off contact), yielding up to two estimates per cell. The resulting velocities for all conditions are presented in Figure 5B. In each condition, the in-contact velocities were consistently lower than those of off-contact cells, regardless of antibody presence or type. This difference was always significant, with a small effect size for wildtype targets (Cliff's Delta > 0.147) and a large effect size for HER2+ targets (Cliff's Delta > 0.474). The lowest in-contact velocities were

observed in the presence of antibodies, showing a significant drop from the target-specific control, with medium effect sizes for the WT bsAbs and HER2+ CE4-28, and a large effect size for HER2+ CE4-21. However, we did not detect any differences in the velocity distributions between the two antibodies for each cell type separately.

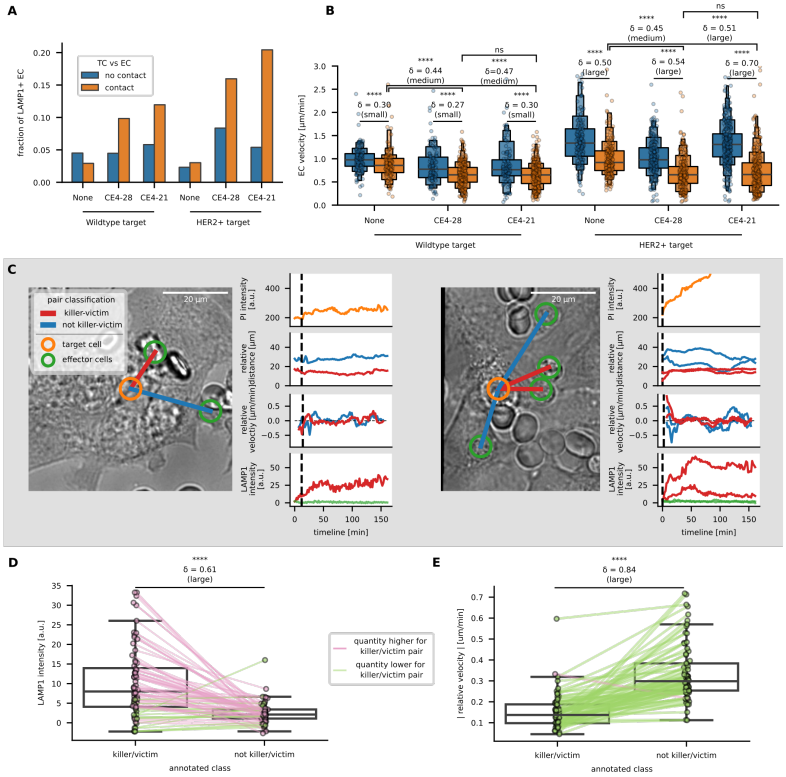

Fig. 5 Effector-target dynamic interactions. For low effector cell density and sufficient frame rate, effector cells can be tracked and dynamic quantities can be measured for effector or effector-target interactions. A. Fraction of cells positive for LAMP1 for different bsAb conditions, split between effector in contact or not with targets (at all time points). B. Average effector velocity for different bsAb conditions, split between effector in contact or not with targets (2 points max per effector). C. Examples of killer-victim identification with one (left) or two (right) killers. One target cell (center) is connected to effector neighbors via colored segments. Dynamic effector-target interaction monitoring includes PI signal of target cell, relative distance and relative velocity between target and effector, as well as LAMP1 signal in effector neighbors. D, E. Characteristic parameters for killer/victim and non-killer/victim pairs. Effector cells are manually annotated as potential killer or not. Each point represents one victim, and the reported value represents the average of the parameter for all neighbors in the given class. D. LAMP1 intensity. E. Relative effector-target velocity.
Video: cell_interactions.mp4

The neighborhood computation generates effector-target cell pairs, enabling detailed analysis of their interactions. First, we measured pair-specific features,

including relative distance and angle, along with their time derivatives. Each cell pair is treated as a single entity that can be classified or associated with dynamic events. To facilitate this analysis, we developed a viewer for cell pairs. In this viewer, clicking on a cell within the reference population (targets) displays selectable segments that link the reference cell to its neighboring effector cells. Upon selecting a pair, time series analysis becomes available, as illustrated in Figures 5C. For example, the PI intensity of the reference cell, indicating cell death at 5 minutes, is plotted alongside the relative distance, relative velocity of neighboring effector cells (highlighting the selected cell in red), and the LAMP1 signal of these effector cells. Among the neighboring cells, only the selected effector shows a strong LAMP1 signal that increases shortly after the target cell death and remains elevated until the end of the observation period.

Using time-lapse images, we sought to identify "killer-victim" pairs. To achieve this, an expert annotated, for each neighborhood containing a dead target cell, the most likely NK cell responsible for killing it, forming a "killer-victim" pair. The annotation was performed using the cell pair viewer mentioned earlier using previously determined target cell death events and a manual classification of the immobilized effector cells as color cues (Video cell_interactions.mp4). This identification was based exclusively on the brightfield movie, with the expert blinded to LAMP1 and other effector fluorescent signals. The expert focused on effector cells exhibiting prolonged, restricted movement in contact with the target cell, hypothesized to reflect direct cell-cell contact (synapse). Effector cells that arrived post-target cell death were excluded from consideration. In cases where multiple cells in the same neighborhood displayed killer-like behavior, each was annotated as a killer-victim pair. Given the complexity of this task, no precise event time could be annotated. In Figures 5D-E, we represent the time-averaged relative velocity and LAMP1 expression for each neighborhood, categorized by killer-victim classification, as paired boxplots. Results indicate that LAMP1 expression was significantly higher in killer-victim pairs, while relative velocity was significantly lower, with both showing a large effect size (Cliff's Delta > 0.474).

Discussion

Here we developed a new analysis tool to study time-dependent multichannel microscopy data from single-cell to cell ensemble scale. It integrates original methods for event detection and cell-pair analysis with established methods for cell segmentation and tracking [35, 36, 41]. Although the pipeline steps are primarily sequential (see Fig. 1, S7) and can be performed independently with different tools, we demonstrate how integrating them within a unified, interactive software environment enhances data exploration and facilitates the analysis of dynamic cell interactions in large datasets.

Celldetective demonstrated its capacity to manage datasets of hundreds of gigabytes, generating high-quality plots that include hundreds of single-cell traces and data points. As a standalone application, it empowers biology experts to analyze single-cell data, annotate labels and events, and train models to automate tasks without requiring coding skills—similar to recent advances for fixed images [54]. Celldetective integrates the open-source annotation tool napari for label correction and introduces

unique tools for event annotation and pair classification. The software combines traditional threshold-based image and signal analysis methods with Deep-learning-based approaches, which can be used complementarily for enhanced results.

We showed how recording multivariate time series may reveal multiple phenomena occuring during the same event. For example, cell death, monitored through an increase in PI fluorescence, was observed alongside apparent nuclear shrinkage (see Fig. 3C). We interpret this as cell de-adhesion upon death, releasing the pushing pressure on the nucleus and allowing its axial shape relaxation [68]. In immunotherapy assays involving human primary cells, we prioritized a fluorescence-based labeling strategy that avoids genetic modification. We also noticed that MCF7 cell line, used here as target, is notoriously challenging to segment using only Brightfield imaging without fluorescent labeling [37, 39]. Due to the exchange of fluorescent dyes between cell populations and cell lysis during the assay, we observed time-dependent staining and overlapping fluorescence signals across three channels. Along with significant size disparities between effector and target cells (or between hovering and spread cells in RICM), this complexity reduced the efficiency of generalist deep-learning segmentation models. To address this, we trained custom models within the software, using StarDist for target nuclei segmentation and Cellpose for effector cells. Performance improved significantly with the simultaneous use of multiple input channels (see Fig. 3B). This approach also benefited event detection: training a model on both PI and nuclear size time series enhanced the event classification performance on the two most important classes for survival studies (see Fig. 3D).

Our spatially resolved immunotherapy assay documents the effect of heterogeneity in target cell density. Indeed, we observed how the high density of target cells reduces their ADCC killing rate, suggesting an apparent protective effect of close target neighbors (see Fig. 3G).

Immune cells function through transient and weak contacts to take rapid decisions [9]. We demonstrate the power of high throughput imaging and analysis to explore such mechanisms. In a cell surface assay, we measure by interference microscopy the decision time for NK cells to spread on an antigen surface in the presence of bispecific antibody. Celldetective provides a high statistical power in this assay as compared to earlier versions of it [62]. Thus, we observed differences in NK response to bispecific antibodies concentration in the minute range, which could not be resolved yet for other systems like TCR-pMHC [69]. Here, the detection of cell sharp shape change like adhesion and spreading could be further enhanced by combining RICM with Brightfield imaging, since each imaging modality exhibit a contrast specific of each cell state [61].

In a co-culture immunotherapy assay, the distribution of fluorescent antibody on effectors can be analyzed in a static way, if the cells can not be tracked, for example at high density. We tested whether we could retrieve the CE4-21/contact condition Ab fluorescence signal by summing up the CE4-21/no-contact and CE4-X/contact signals. Interestingly, the sum of signals was always smaller than the CE4-21/contact signal. Hypothesizing that the CE4-X Ab had the same affinity to the target cells as the CE4-21 bsAb and that the amount of fluorophore was identical, we speculated this

might be due to a bsAb recruitment at the effector-to-target junction, thus explaining the stronger signal measured.

We provide information similar to flow cytometry data gating for positive and negative cells. Proximity between effector and target provides an additional gating out of reach for traditional flow cytometry, and showing some clear differences in LAMP1 signal and relative velocity. We introduce a scheme analysis based on classes, which allow quantification of subpopulation based on arbitrary measured signal values. Additionally, instantaneous signal can be complement by cell integrated signal when tracking is performed. To go further into the analysis of effector-target dynamic interactions, we addressed the question of killer:victim pair identification. The strategy consists in collectiong relative measurements like velocity and manually annotating the potential killer for each target. Our data are consistent with one or several killers. The most prominent parameters for killer identification are relative velocity and LAMP1 signal.

As a perspective, further work is required to analyze automatically the dynamic signaling and provide more robust prediction. Celldetective offers in principle the complete environment for such an advanced analysis, as demonstrated with the death time automatic detection.

For its applicability, Celldetective does not require coding skills. It was tested by graduate students from our labs with diverse backgrounds in biophysics, cell biology and immunology. Its release is accompanied by examples and a complete documentation. Software maintenance and user assistance are offered via github platform and a professional development team (https://github.com/centuri-engineering). One highlight of Celldetective is to offer alternative methods, in particular for cell segmentation, so that the user can maximize the outcome. In order to guide the user for software applicability and workflow, we propose a decision tree, visible as question marks in the interface, to assist in choosing between the different options.

Target segmentation was achieved through nuclear staining and using the StarDist method [35], providing robust target cell counts and precise death event detection. However, an additional membrane stain could enhance boundary delineation, potentially improving neighborhood estimates.

The experimental systems analyzed here are largely two-dimensional, but at the cellular scale, exhibit a three-dimensional aspect. Future software expansions could incorporate 2.5D or 3D sequence analysis. Currently, to our knowledge, only proprietary solutions are offered and exploited in immunotherapy assays [26]. Notably, cell-interaction studies benefit from higher time resolution, which may limit compatibility with extensive 3D analysis.

The methodologies we demonstrate here should adapt well to commercial high-throughput automated microscopes for long-term cell co-culture studies [39], for which no efficient analysis solutions are available, to our knowledge. A distinctive aspect of our approach is the use of compact, efficient models that are user-trainable on a single GPU setup. This contrasts with approaches relying on large-scale databases [39] and extensive DL models [70]. Moreover, the software's integrated visualization and

annotation features encourage meticulous review of segmentation and tracking results, enhancing confidence in the analysis.

Convolutional models used by the software, such as U-Net and ResNet, are prone to forgetting previously learned tasks upon transfer [71]. To address this, Celldetective allows the addition of the original dataset during transfer from a model we trained. Future extensions could include foundation models like SAM [72] for broader adaptability.

Processing time for segmenting an entire experiment can be non negligible, especially when segmenting two populations. One potential acceleration method could involve combining segmentation with classification [58], although this approach requires validation for a co-culture system, particularly in handling segmentation challenges like screening.

While tracking is highly customizable, fine-tuning it can be complex. To assist users, we provide helper buttons and preconfigured settings for various tracking scenarios. Although direct track correction is currently outside the scope of this software, a related napari plugin from third parties is anticipated soon.

The current event formulation—supporting three classes and one event time—is primarily designed for irreversible events, as in the applications presented. It is not yet optimized for periodic or transitional events, unclear transitions, or reversible events. However, it could be adapted for analyzing cascades of events.

Conclusion

In conclusion, Celldetective is a user-friendly software designed for non-specialists, providing advanced cell-scale analysis for large cell populations. Combining high time-resolution with robust statistical capabilities, we show the potential to uncover new fundamental parameters characterizing dynamic interactions between immune and tumor cells. We demonstrated the efficiency of Celldetective through two applications in the context of immunotherapy by isolating time-dependent cell-scale parameters and paired-interactions, in high cell-density environment. We believe that such approach holds great potential for enhancing the design and discovery of drugs in a more powerful and rational manner, while also finding broader applications in fundamental studies of cell-cell interactions in developmental biology, microbiology or neurosciences.

Materials and Methods

Antibody design and production

The bispecific antibody (bsAb) C7b-21 (or CE4-21, CE4-28) is a fusion of two single domain antibodies (sdAb, also called nanobodies), sdAb C7b (or CE4) targeting against Human epidermal growth factor receptor-2 (HER-2/neu or ErbB2) [73] and sdAb C21 (or C28) targeting human CD16 (FcγRIII), using the human CH1/Ck heterodimerization motif, corresponding to the bispecific Fab (bsFab) format [74]. bsFab CE4-28 was produced by co-transfection of two plasmids using the mammalian transient system Expi293 (Thermofisher) and purified as previously described [75]. For experiments in Fig. 4 bsAb CE4-21 and control antibody CE4-X where specifically

labelled with Atto647 dye using transglutaminase reaction (Zedira, Darmstadt, Germany).

Cell lines culture, effector extraction and phenotyping

Modified MCF7-HER2+ cells were stably transfected from MCF7 cell line to overexpress HER2 receptors. Determination of HER-2 levels on the cells was performed by flow cytometry with Herceptin antibody and a secondary fluorescent anti-human antibody. Fluorescence intensity was determined and correlated with HER-2 levels. Cells were maintained in RPMI 1640 media (Gibco, Life Technologies), supplemented with 10% of Fetal Bovine Serum, FBS (Gibco, Life Technologies), 50 mg/mL of hygromycin as an antibiotic resistance selection. Cells were amplified three times per week and keep in the incubator at 37°C under 5% CO_2 atmosphere.

Primary human NK cells. NK cells were isolated as described in [61]. Briefly, blood samples were obtained from the Etablissement Francais du Sang (Marseille, France), using the MACSxpress whole-blood human NK cell isolation kit (Miltenyi Biotec, Bergisch Gladbach, Germany) a negative selection was performed. The characterization of the sorted cells was determined by flow cytometry with anti-CD16, anti-CD3 and anti-CD56 antibodies. Cells were maintained in RPMI 1640 medium and 10% FBS at 37°C, 5% CO_2 and used in the following 24 hours.

Cell-surface assay

Freshly isolated primary human NK cells were used in this experiment. A concentration of 200 000 cells/mL was added to an uncoated eight-well chambered polymer coverslip-bottom from Ibidi (80821, Ibidi, Munich). For surface preparation, the Ibidi wells were initially rinsed with PBS, followed by incubation in a solution of Biotin-labeled bovine albumin (A8549-10MG, Sigma) diluted in PBS at 100 μg/mL for 30 min at room temperature (RT) with agitation. To remove non-adsorbed BSA-biotin, the wells were rinsed four times with PBS. Afterwards, the wells were incubated in a 10 μg/mL Neutravidin solution (31000, Thermo Scientific) diluted in PBS for 30 min at RT with agitation. After a four-time PBS wash, the wells received an Her2/ERBB2 Protein solution (10004-H27H-B, Sinobiological) diluted in 0.2% BSA at 10 nM/mL for 30 minutes at RT with agitation, followed by another four-time PBS wash. The Ibidi chamber was then placed under a microscope at 37°C. Prior to the experiment, the NK were incubated with the desired concentration of bsFab (C7b-21) during 30 min at 37°C. They were then injected in the sample.

Cell-surface contact and cell spreading dynamics were observed through reflection interference contrast microscopy (RICM), a technique sensitive to cell-surface distance. The RICM setup is described in [64]. An antiflex Zeiss objective (NA = 1.25) was used with a green LED light source (λ= 546 nm) and a 14-bit CCD detector (Andor iXonEM, Oxford instruments). This configuration allows live cell observations at 37°C. Images were acquired after cell deposition in the device. To measure the decision time between cell landing and spreading, and the spreading kinetics of NK cells, multiple fields of view were selected (sixteen per condition) and subjected to cyclic imaging over a 10-minute interval, facilitated by a motorized stage from Physik Instrumente,

Germany. The temporal interval between successive images of a given field typically ranged from 15 to 20 seconds.

Cell-cell assay

MCF7-Mod cells, expressing HER2 at a surface density of *ca.* 500 molec/μm^2 [67], were used as target cells. 80 000 cells/well were seeded in an 8-well chamber μ-Slide, polymer bottom, TC treated from Ibidi (Munich, Germany). Cells were cultured overnight in RPMI complemented media and allowed to reach exponential growth (at least 18 h) under 37°C and 5% of CO_2. Next day media was aspirated and cells were incubated with Hoechst 33342 in colorless RPMI media (5 μg/mL), at 37°C during 10 min. After that, Hoechst solution were removed and the cells were rinsed 3 times with warm colorless RPMI media complemented with 10% of FBS (300 μL/well). Cells were put back in the incubator. NK primary cells were stained with CFSE dye according to the manufacturer instructions (CFSE CellTrace, Thermofisher). 2.5 M cells were centrifuged at 1500 rpm for 5 min; the supernatant was discarded and the cells were incubated with 2.5 mL of CFSE diluted in PBS for 20 min at 37°C. After that time 12.5 mL of colorless RPMI + 10% FBS were added to the cells and incubated for 5 minutes more. Then the cells were centrifuged at 1500 rpm for 5 min. Cells were resuspended in complemented media and put back in the incubator.

Dilutions of the bsAb CE4-28 were prepared to obtain a final concentration of 1, 10 and 100 pM. The proper bsAb solution was added to each well (2 μg/mL) where the target cells were previously marked with Hoechst and incubated at 37°C during 20 min. After that time, Propidium Iodide (Sigma) was added in each well condition, then the cells were taken from the incubator and NK cells were added to each well to have a final effector to target (E:T) ratio of 2.5. The slide was then placed in the Zeiss AxioObserver epifluorescence microscope with temperature control at 37°C. The image acquisition consists of taking 5 to 9 fields per well, with a 20x / 0.4 objective (pixel size 0.31 μm) each field was imaged using transmitted light (Bright field), Zeiss filter set 38 (CFSE), Zeiss filter set # 49 (Hoechst) and Zeiss filter set # 25 HE (Propidium iodide). Each position was imaged during 2-3 hours with approx. 3 min between each frame.

For NK tracking, the observation was realized with a 40x / 1.3 Oil Dic (UV) objective (pixel size 0.157 μm) and at 1.73 min per frame. Additionally, the E:T ratio was set to 1:1. For monitoring degranulation, fluorescent anti-LAMP1 (Biolegend APC labelled Clone. H4A3 Cat. 328619) antibody were added at 5 μl for 1 M NK cells.

Hardware and software

Software development and analysis was carried on an Intel-core i9 CPU, NVIDIA RTX 3070 GPU, 16 Go of RAM, Ubuntu 20.04 desktop. The software was extensively tested on an Intel-core i9 CPU desktop running on Windows 11, an Intel-core i7-8565U laptop running on Windows 11, and an older Intel(R) Core(TM) i5 CPU 750 @ 2.67 GHz desktop computer running on Ubuntu 20.04.

The software is a python package augmented with a PyQt5 user-interface. The UI occasionally integrates Matplotlib canvases for image, animation and plot purposes.

The GUI styling is based on Material Design. Each of the processing modules (segmentation, tracking, measurement, event detection, pair analysis) triggers a subprocess that applies to a single movie at a time. Upon completion of the subprocess, CPU and GPU memories are fully released, allowing to reiterate the process on the next movie or to unfreeze the GUI. Multi-threading was implemented where it is applicable and can be configured in the software.

For each processing module, an output (image, table) is written on the disk (in the experiment folder) and can be read as the input to the next module. This approach provides a regular and automatic saving of the data and the modularity allows flexibility in the input data that can be intuitively imported from external sources (ImageJ, Cellpose UI...). In more detail, the segmentation module outputs mask images (frame by frame). The tracking module outputs a trajectory table for the cell population of interest. The measurement and event detection modules build on the trajectory tables by adding columns. The neighborhood module adds columns to the trajectory tables and saves a pickle file with a nested-dictionary table with information about the neighbors at each time point.

Celldetective is routinely tested against Python versions 3.9-3.11 on Windows and Linux platforms, with procedural and graphical unitary tests.

Analysis

Software

Segmentation model training: Each channel's normalization can be independently adjusted using either percentile or absolute normalization. For RICM images, which are background-corrected with intensities centered around 1, an absolute normalization range of 0.75 to 1.25 was adopted. In contrast, fluorescence images—where light source power and exposure often vary across experiments—use percentile normalization, typically set between the 0.1-th and 99.99-th percentile for each image.

During training, images in the training set are randomly augmented with operations such as flips and lateral shifts. Each input channel can undergo independent intensity adjustments, including blurring (random sigma between 0 and 4 px), physical noise addition (Gaussian, local variance, Poisson, and speckle), and random deactivation of channels (excluding the primary input channel), encouraging the model to learn redundancy across channels. StarDist models are trained for around 300 epochs with a learning rate of approximately 10^{-4} and a typical batch size of 8, while Cellpose models are trained over roughly 3000 epochs with a learning rate near 10^{-2} and a similar batch size.

To improve the annotation experience in napari, we developed a plugin that addresses common annotation errors identified with our expert annotators. The plugin detects repeated label values by comparing cell bounding boxes with mask areas, interpreting significant differences as multiple cells sharing the same label. Noncontiguous objects are automatically separated and relabeled, while small objects (less than 9 px^2) are filtered out. The plugin also reassigns label values sequentially from 1 to the total number of objects, manages annotation naming and storage,

and appends experiment metadata to each annotation, enabling precise tracking of annotation origin and context.

Event detection: The event detection system comprises two sequential ResNet-like models with a shared backbone but distinct heads tailored to different tasks: classification and regression (see Fig. S10). Input time series are structured as tensors of shape $(T \times n_{\text{channels}})$, where n_{channels} represents the number of coupled time series (or channels) and T is an arbitrary maximum time series length, typically set to 128 frames. The input tensor is initially processed by a 1D convolution layer with a $(1,)$ kernel to expand it into 64 filters. It then passes through two 1D-ResBlocks, each with a $(8,)$ kernel and 64 filters, followed by a max-pooling layer (size 2) that doubles the number of filters to 128. The tensor continues through two additional 1D-ResBlocks before undergoing a global average pooling operation. A dense layer with 512 neurons collects the convolutional information, followed by a dropout layer with a 50 % dropout rate. The final layers differ by model task: for classification, a layer with three neurons and softmax activation distinguishes between three classes; by convention "event observed", "no event observed", and "event left censored"; for regression, a single neuron with linear activation predicts t_{event}. The models are trained for 300 and 600 epochs, respectively, using the Adam optimizer with a user-controlled learning rate (typically 10^{-4}, unless mentioned otherwise). For classification, categorical cross-entropy loss is minimized, with class weights introduced to mitigate class imbalance. For regression, the mean squared error is minimized. The batch size, usually set to 64 or 128 depending on the dataset size, is user-controlled. Only cells classified as the first class ("event observed") proceed to the regression model during both training and inference.

Cell-surface assay

Processing: A RICM background for each well of the cell-surface assay was reconstructed using the model-free background estimate method in Celldetective (Supplementary Fig. S8B). The reconstructed backgrounds were optimized and divided to the RICM images, yielding float intensities centered around 1. The traditional segmentation pipeline consisted of two mathematical operations on the pixels (subtracting one and taking the absolute value) and a Gaussian filter (kernel of 0.8 pixels), followed by thresholding, watershed and automatic removal of non-lymphocyte objects. The pipeline was defined with the dedicated Celldetective module (Supplementary Fig. SS11). To track the cells, the bTrack configuration was tuned to increase the isotropic spatial bin size to consider hypotheses (`dist_thresh` = 99.99), so that hypothesese could be generated for each tracklet. The branching, apoptosis and merging tracklet reconnection hypotheses were disabled and the segmentation miss rate reduced to 1 %. The position-based intensity measurements were performed in a circle of 2 μm diameter centered around the cell positions.

Segmentation benchmark: To use the Cellpose *cyto3* model, we passed a diameter value of 15 μm, a `cellprob_threshold` of 0 and `flow_threshold` of 0.4. For each sample in the test set, the lymphocyte detection accuracy was defined as: $DA = \text{TP}/(\text{TP} + \text{FP} + \text{FN})$, with TP the number of lymphocytes predicted, FP the number of non-lymphocyte objects detected and FN the number of lymphocytes missed. A

detection was accepted when the intersection over union (IoU) reached at least 0.1. The segmentation quality was defined as the IoU between the ground truth and predicted masks when they could be matched (TP detections). Since hovering cells had an ill-defined area, the segmentation quality was only computed for the subset of spread cells. The scores reported in Fig. 2 are the average over all test samples of the lymphocyte detection accuracy and the segmentation quality. The average score was defined as the average of these two scores for each segmentation method. The benchmark was done in a Jupyter Notebook.

Spreading rate: For each spread cell, the area was differentiated as a function of timeusing a sliding window of 5 frames (1 min 18 s) looking forward in time: from t_i to t_{i+4} (this was configured graphically in the table exploration feature of Celldetective). The value at the onset of spreading t_{spread} was then extracted for each cell (with a track collapse option in the software) and plotted.

Cell-cell assay

Processing: The fluorescent bsAb and LAMP1 channels were corrected for the background using the same paraboloid fit technique described in Supplementary Fig. S8A. The fitted background for each image was subtracted to the original image, without clipping. The movies from the LAMP1 experiment were aligned prior to analysis with the SIFT multichannel registration plugin in Fiji (to be able to investigate effector cell velocities). The macro used to align the movies in a Celldetective experiment project is available in the documentation. For the interaction study, some manual corrections of target and effector segmentation results had to be done to achieve an excellent tracking quality for both populations and study their interactions. To measure effector cell contact with the target cells, an isotropic neighborhood of radius 20 μm was computed. Effector cell velocity was computed over a sliding window of 3 frames (5.19 min) centered on the current time (from t_{i-1} to t_{i+1}).

Segmentation benchmark: Nuclear detection accuracy was defined in the same way as the lymphocyte detection accuracy in the cell-surface assay. To use the Cellpose *nuclei* model, we set the diameter to 22 μm, the `cellprob_threshold` parameter to 0.0 and the `flow_threshold` parameter to 0.4. The segmentation quality is computed over all nuclei. As before, the scores reported in Fig. 3 are the average over all test samples of the detection accuracy and segmentation quality. The average score was defined as the average of these two scores for each segmentation method.

Death event detection benchmark: the event detection models we present were trained on the `db-si-NucPI` dataset available in Zenodo with a 20 % validation split and 10 % test split, randomized at each training. For each tested combination of batch size (BS $\in [64, 128, 256]$) and learning rate ($\alpha \in [10^{-4}, 10^{-3}, 10^{-2}, 10^{-1}]$), we trained 10 event detection models for 300 epochs with the two different input approaches (PI time series alone or PI + nuclear area time series). The time series were normalized with a percentile normalization (0.1 % and 99.9 %) and clipping. The model input tensor length was set to 128 frames. For the hyperparameters that achieved the best average performance (here BS = 64 and $\alpha = 10^{-4}$), we picked the best event detection

model produced out of the 10 for the benchmark of Fig 3D. This benchmark was performed on a separate test set, identical for all methods. The annotations came from 3 movies, two of which belonged to experiments never seen by the models. The third is from a position adjacent to a position seen by the models. It was selected due to its over-representation of cells that are already dead from the beginning, or dying at the very beginning, which are very rare in most experiments. The benchmark was done in a Jupyter notebook.

Simulation The Monte-Carlo simulation for the sum of bsAb fluorescence signals and its comparison with the other conditions was performed in a Jupyter Notebook with in-house code and functions from the Celldetective package. This notebook allowed us to produce figures 4D and Figure Supp S14.

Statistics

Statistical tests: Since for all multi-condition comparisons at least one distribution was not normally distributed, we assessed statistical difference using the nonparametric two-sample Kolmogorov-Smirnov one-sided test (Python package `scipy.stats.ks_2samp`). P-values were converted into star notations following the GraphPad convention: $P > 0.05$: ns, $P < 0.05$: *, $P < 0.01$: **, $P < 0.001$: ***, $P < 0.0001$: ****.

Effect sizes: For statistically significant differences, we computed Cliff's Delta to report the effect size (Python package `cliffs-delta`). We followed the conventions of the package to convert the effect size value into a qualitative effect: $\delta < 0.147$: negligible, $\delta < 0.33$: small, $\delta < 0.474$: medium, $\delta > 0.474$: large.

Plots

Most plots presented in this article were generated within Celldetective using the `matplotlib` and `seaborn` packages. Notable exceptions include the benchmarks (segmentation scores, confusion matrix and correlation plots). Composition was done on Inkscape to add statistical tests and effect sizes or merge separate plot layers.

Acknowledgments

We thank Cristina Gonzalez and Maddy Messa N'Dong for preliminary experiments; Juliette Prothon for producing and labelling the bispecific antibodies; Adrien Aimard, Dominique Touchard, Martine Biarnes for excellent technical support; Pierre-Henri Puech and Thierry Galliano for fruitful discussions. The project leading to this publication has received funding from France 2030, the French Government program managed by the French National Research Agency (ANR-16-CONV-0001) and from Excellence Initiative of Aix-Marseille University - A*MIDEX AMX-21-IET-017, as well as AMIDEX Emergence Innovation (project ForSelecAntibody), Plan Cancer PhysCancer program (project ComPhysAb) and ANR-22-CE09-0014. .

References

[1] Rafelski, S. M. & Theriot, J. A. Establishing a conceptual framework for holistic cell states and state transitions. *Cell* **187**, 2633–2651 (2024).

[2] Kramer, B. A., Sarabia del Castillo, J. & Pelkmans, L. Multimodal perception links cellular state to decision-making in single cells. *Science* **377**, 642–648 (2022).

[3] Bagheri, N., Carpenter, A. E., Lundberg, E., Plant, A. L. & Horwitz, R. The new era of quantitative cell imaging—challenges and opportunities. *Molecular Cell* **82**, 241–247 (2022).

[4] Malissen, B. & Bongrand, P. Early T cell activation: Integrating biochemical, structural, and biophysical cues. *Annual review of immunology* **33**, 539–561 (2015).

[5] Belardi, B., Son, S., Felce, J. H., Dustin, M. L. & Fletcher, D. A. Cell–cell interfaces as specialized compartments directing cell function. *Nature Reviews Molecular Cell Biology* **21**, 750–764 (2020).

[6] Kiesgen, S., Messinger, J. C., Chintala, N. K., Tano, Z. & Adusumilli, P. S. Comparative analysis of assays to measure CAR T-cell-mediated cytotoxicity. *Nature Protocols* **16**, 1331–1342 (2021).

[7] Ginhoux, F., Yalin, A., Dutertre, C. A. & Amit, I. Single-cell immunology: Past, present, and future. *Immunity* **55**, 393–404 (2022).

[8] Limozin, L. & Puech, P.-H. Membrane Organization and Physical Regulation of Lymphocyte Antigen Receptors: A Biophysicist's Perspective. *The Journal of Membrane Biology* **252**, 397–412 (2019).

[9] Bongrand, P. Understanding How Cells Probe the World: A Preliminary Step towards Modeling Cell Behavior? *International Journal of Molecular Sciences* **24**, 2266 (2023).

[10] Sengupta, K., Dillard, P. & Limozin, L. Morphodynamics of T-lymphocytes: Scanning to spreading. *Biophysical Journal* S0006349524001577 (2024).

[11] Eulenberg, P. *et al.* Reconstructing cell cycle and disease progression using deep learning. *Nature Communications* **8**, 463 (2017).

[12] Shetab Boushehri, S. *et al.* Explainable machine learning for profiling the immunological synapse and functional characterization of therapeutic antibodies. *Nature Communications* **14**, 7888 (2023).

[13] German, Y. *et al.* Morphological profiling of human T and NK lymphocytes by high-content cell imaging. *Cell Reports* **36**, 109318 (2021).

[14] Chandrasekaran, S. N., Ceulemans, H., Boyd, J. D. & Carpenter, A. E. Image-based profiling for drug discovery: Due for a machine-learning upgrade? *Nature Reviews Drug Discovery* **20**, 145–159 (2021).

[15] Olofsson, P. E. *et al.* Distinct Migration and Contact Dynamics of Resting and IL-2-Activated Human Natural Killer Cells. *Frontiers in Immunology* **5** (2014).

[16] Lu, H. *et al.* TIMING 2.0: High-throughput single-cell profiling of dynamic cell–cell interactions by time-lapse imaging microscopy in nanowell grids. *Bioinformatics* **35**, 706–708 (2019).

[17] Alieva, M., Wezenaar, A. K. L., Wehrens, E. J. & Rios, A. C. Bridging live-cell imaging and next-generation cancer treatment. *Nature Reviews Cancer* (2023).

[18] Vanherberghen, B. *et al.* Classification of human natural killer cells based on migration behavior and cytotoxic response. *Blood* **121**, 1326–1334 (2013).

[19] Wiggins, L. *et al.* The CellPhe toolkit for cell phenotyping using time-lapse imaging and pattern recognition. *Nature Communications* **14**, 1854 (2023).

[20] Salles, A. *et al.* Barcoding T Cell Calcium Response Diversity with Methods for Automated and Accurate Analysis of Cell Signals (MAAACS). *PLoS Computational Biology* **9**, e1003245 (2013).

[21] This, S., Costantino, S. & Melichar, H. J. Machine learning predictions of T cell antigen specificity from intracellular calcium dynamics. *Science Advances* **10**, eadk2298 (2024).

[22] Sità, L. *et al.* A deep-learning approach for online cell identification and trace extraction in functional two-photon calcium imaging. *Nature Communications* **13**, 1529 (2022).

[23] Lee, M. *et al.* Deep-learning-based three-dimensional label-free tracking and analysis of immunological synapses of CAR-T cells. *eLife* **9**, e49023 (2020).

[24] Ichise, H. *et al.* Functional visualization of NK cell-mediated killing of metastatic single tumor cells. *eLife* **11**, e76269 (2022).

[25] Liu, B. *et al.* Deep Learning–Based 3D Single-Cell Imaging Analysis Pipeline Enables Quantification of Cell–Cell Interaction Dynamics in the Tumor Microenvironment. *Cancer Research* **84**, 517–526 (2024).

[26] Dekkers, J. F. *et al.* Uncovering the mode of action of engineered T cells in patient cancer organoids. *Nature Biotechnology* **41**, 60–69 (2023).

[27] Roudot, P. *et al.* U-track3D: Measuring, navigating, and validating dense particle trajectories in three dimensions. *Cell Reports Methods* **3**, 100655 (2023).

[28] Berg, S. *et al.* Ilastik: Interactive machine learning for (bio)image analysis. *Nature Methods* **16**, 1226–1232 (2019).

[29] Moen, E. *et al.* Deep learning for cellular image analysis. *Nature Methods* **16**, 1233–1246 (2019).

[30] Arzt, M. *et al.* LABKIT: Labeling and Segmentation Toolkit for Big Image Data. *Frontiers in Computer Science* **4**, 777728 (2022).

[31] Jan, M., Spangaro, A., Lenartowicz, M. & Mattiazzi Usaj, M. From pixels to insights: Machine learning and deep learning for bioimage analysis. *BioEssays* **46**, 2300114 (2024).

[32] Shroff, H., Testa, I., Jug, F. & Manley, S. Live-cell imaging powered by computation. *Nature Reviews Molecular Cell Biology* (2024).

[33] Vicar, T. *et al.* Cell segmentation methods for label-free contrast microscopy: Review and comprehensive comparison. *BMC Bioinformatics* **20**, 360 (2019).

[34] Falk, T. *et al.* U-Net: Deep learning for cell counting, detection, and morphometry. *Nature Methods* **16**, 67–70 (2019).

[35] Weigert, M., Schmidt, U., Haase, R., Sugawara, K. & Myers, G. *Star-convex Polyhedra for 3D Object Detection and Segmentation in Microscopy*, 3655–3662 (IEEE, Snowmass Village, CO, USA, 2020).

[36] Stringer, C., Wang, T., Michaelos, M. & Pachitariu, M. Cellpose: A generalist algorithm for cellular segmentation. *Nature Methods* **18**, 100–106 (2021).

[37] Pachitariu, M. & Stringer, C. Cellpose 2.0: How to train your own model. *Nature Methods* **19**, 1634–1641 (2022).

[38] Greenwald, N. F. *et al.* Whole-cell segmentation of tissue images with human-level performance using large-scale data annotation and deep learning. *Nature Biotechnology* **40**, 555–565 (2022).

[39] Edlund, C. *et al.* LIVECell—A large-scale dataset for label-free live cell segmentation. *Nature Methods* **18**, 1038–1045 (2021).

[40] Wen, C. *et al.* 3DeeCellTracker, a deep learning-based pipeline for segmenting and tracking cells in 3D time lapse images. *eLife* **10**, e59187 (2021).

[41] Ulicna, K., Vallardi, G., Charras, G. & Lowe, A. R. Automated deep lineage tree analysis using a Bayesian single cell tracking approach. *Frontiers in Computer Science* **3**, 734559 (2021).

[42] Ershov, D. *et al.* TrackMate 7: Integrating state-of-the-art segmentation algorithms into tracking pipelines. *Nature Methods* (2022).

[43] Cuny, A. P., Ponti, A., Kündig, T., Rudolf, F. & Stelling, J. Cell region fingerprints enable highly precise single-cell tracking and lineage reconstruction. *Nature Methods* **19**, 1276–1285 (2022).

[44] Soelistyo, C. J., Ulicna, K. & Lowe, A. R. Machine learning enhanced cell tracking. *Frontiers in Bioinformatics* **3**, 1228989 (2023).

[45] Ollion, J., Maliet, M., Giuglaris, C., Vacher, É. & Deforet, M. DiSTNet2D: Leveraging Long-Range Temporal Information for Efficient Segmentation and Tracking. *PRX Life* **2**, 023004 (2024).

[46] Lugagne, J.-B., Lin, H. & Dunlop, M. J. DeLTA: Automated cell segmentation, tracking, and lineage reconstruction using deep learning. *PLOS Computational Biology* **16**, e1007673 (2020).

[47] Padovani, F., Mairhörmann, B., Falter-Braun, P., Lengefeld, J. & Schmoller, K. M. Segmentation, tracking and cell cycle analysis of live-cell imaging data with Cell-ACDC. *BMC Biology* **20**, 174 (2022).

[48] Schwartz, M. S. *et al.* Caliban: Accurate cell tracking and lineage construction in live-cell imaging experiments with deep learning (2023).

[49] Schindelin, J. *et al.* Fiji: An open-source platform for biological-image analysis. *Nature Methods* **9**, 676–682 (2012).

[50] De Chaumont, F. *et al.* Icy: An open bioimage informatics platform for extended reproducible research. *Nature Methods* **9**, 690–696 (2012).

[51] McQuin, C. *et al.* CellProfiler 3.0: Next-generation image processing for biology. *PLOS Biology* **16**, e2005970 (2018).

[52] Gómez-de-Mariscal, E. *et al.* DeepImageJ: A user-friendly environment to run deep learning models in ImageJ. *Nature Methods* **18**, 1192–1195 (2021).

[53] Stirling, D. R. *et al.* CellProfiler 4: Improvements in speed, utility and usability. *BMC Bioinformatics* **22**, 433 (2021).

[54] Körber, N. MIA is an open-source standalone deep learning application for microscopic image analysis. *Cell Reports Methods* **3**, 100517 (2023).

[55] Windhager, J. *et al.* An end-to-end workflow for multiplexed image processing and analysis. *Nature Protocols* (2023).

[56] von Chamier, L. *et al.* Democratising deep learning for microscopy with ZeroCostDL4Mic. *Nature Communications* **12**, 2276 (2021).

[57] Edelstein, A. D. *et al.* Advanced methods of microscope control using μManager software. *Journal of Biological Methods* **1**, 10 (2014).

[58] Pang, M., Roy, T. K., Wu, X. & Tan, K. CelloType: A Unified Model for Segmentation and Classification of Tissue Images (2024).

[59] Juppet, Q. *et al.* Deep Learning Enables Individual Xenograft Cell Classification in Histological Images by Analysis of Contextual Features. *Journal of Mammary Gland Biology and Neoplasia* **26**, 101–112 (2021).

[60] Haralick, R. M., Shanmugam, K. & Dinstein, I. Textural Features for Image Classification. *IEEE Transactions on Systems, Man, and Cybernetics* **SMC-3**, 610–621 (1973).

[61] Gonzalez, C. *et al.* Nanobody-CD16 Catch Bond Reveals NK Cell Mechanosensitivity. *Biophysical Journal* **116**, 1516–1526 (2019).

[62] Robert, P., Limozin, L., Van Der Merwe, P. A. & Bongrand, P. CD8 Co-Receptor Enhances T-Cell Activation without Any Effect on Initial Attachment. *Cells* **10**, 429 (2021).

[63] Turini, M., Chames, P., Bruhns, P., Baty, D. & Kerfelec, B. A FcgammaRIII-engaging bispecific antibody expands the range of HER2-expressing breast tumors eligible to antibody therapy. *Oncotarget* **5**, 5304–5319 (2014).

[64] Limozin, L. & Sengupta, K. Quantitative Reflection Interference Contrast Microscopy (RICM) in Soft Matter and Cell Adhesion. *ChemPhysChem* **10**, 2752–2768 (2009).

[65] Sengupta, K., Aranda-Espinoza, H., Smith, L., Janmey, P. & Hammer, D. Spreading of Neutrophils: From Activation to Migration. *Biophysical Journal* **91**, 4638–4648 (2006).

[66] Dillard, P., Varma, R., Sengupta, K. & Limozin, L. Ligand-Mediated Friction Determines Morphodynamics of Spreading T Cells. *Biophysical Journal* **107**, 2629–2638 (2014).

[67] Gonzalez Gutierrez, C. *et al.* Decoupling individual host response and immune cell engager cytotoxic potency (2024).

[68] Versaevel, M., Grevesse, T. & Gabriele, S. Spatial coordination between cell and nuclear shape within micropatterned endothelial cells. *Nature Communications* **3** (2012).

[69] Brodovitch, A. *et al.* T lymphocytes need less than 3 min to discriminate between peptide MHCs with similar TCR-binding parameters: Cellular immune response. *European Journal of Immunology* **45**, 1635–1642 (2015).

[70] Israel, U. *et al.* A Foundation Model for Cell Segmentation. Preprint, Bioinformatics (2023).

[71] Ma, J. *et al.* The multimodality cell segmentation challenge: Toward universal solutions. *Nature Methods* **21**, 1103–1113 (2024).

[72] Ravi, N. *et al.* SAM 2: Segment Anything in Images and Videos (2024). 2408.00714.

[73] Even-Desrumeaux, K. *et al.* Masked Selection: A Straightforward and Flexible Approach for the Selection of Binders Against Specific Epitopes and Differentially Expressed Proteins by Phage Display. *Molecular & Cellular Proteomics* **13**, 653–665 (2014).

[74] Rozan, C. *et al.* Single-Domain Antibody-Based and Linker-Free Bispecific Antibodies Targeting Fc RIII Induce Potent Antitumor Activity without Recruiting Regulatory T Cells. *Molecular Cancer Therapeutics* **12**, 1481–1491 (2013).

[75] Raynaud, A. *et al.* Anti-NKG2D single domain-based antibodies for the modulation of anti-tumor immune response. *OncoImmunology* **10**, 1854529 (2021).

[76] Barshir, R. *et al.* The TissueNet database of human tissue protein–protein interactions. *Nucleic Acids Research* **41**, D841–D844 (2013).

[77] Caicedo, J. C. *et al.* Nucleus segmentation across imaging experiments: The 2018 Data Science Bowl. *Nature Methods* **16**, 1247–1253 (2019).

[78] Kumar, N. *et al.* A Multi-Organ Nucleus Segmentation Challenge. *IEEE Transactions on Medical Imaging* **39**, 1380–1391 (2020).

[79] Naylor, P., Lae, M., Reyal, F. & Walter, T. Segmentation of Nuclei in Histopathology Images by Deep Regression of the Distance Map. *IEEE Transactions on Medical Imaging* **38**, 448–459 (2019).

Supplementary Tables

Table S2 Generalist Deep-learning segmentation models. This table lists the different generalist models (Cellpose or StarDist) which can be called natively in Celldetective. The sample images are cropped to (200 × 200) px and rescaled homogeneously to fit in the table.

name	modalities	# channels	dataset	sample image
`CP_cyto3`	cytoplasm nucleus	2	Cellpose [37] & user-submitted images	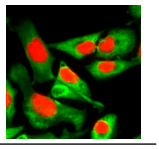
`CP_livecell`	cytoplasm (BF) black	2	LiveCell [39]	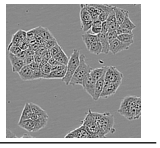
`CP_tissuenet`	cytoplasm nucleus	2	TissueNet[76]	/
`CP_nuclei`	nucleus black	2	?	/
`SD_versatile_fluo`	nucleus	1	subset of DSB 2018 [77]	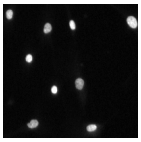
`SD_versatile_he`	H&E RGB	1	MonoNuSeg 2018 [78] TNBC 2018 [79]	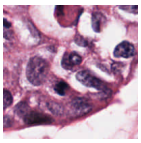

Table S3 MCF7 nuclei segmentation models in the presence of primary NK cells. Each model was trained on the same dataset of ADCC images, picking only the relevant channels.

Name	Channels	Type	Pretrained	Spatial calib. (μm)	sample image
`mcf7_nuc_multimodal`	Hoechst Brightfield CFSE PI	StarDist	None	0.3112	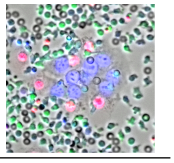
`mcf7_nuc_stardist_transfer`	Hoechst	StarDist	`SD_versatile_fluo`	0.3112	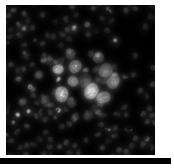

Table S4 Primary NK segmentation models. The models have been trained on a dataset of annotated primary NKs in ADCC images (*primary_NKs_w_MCF7*).

Name	Channels	Type	Pretrained	Spatial calib. (μm)	sample image
`primNK_multimodal`	brightfield CFSE Hoechst	Cellpose	None	0.2178	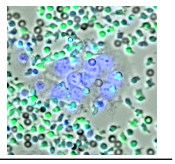
`primNK_cfse`	CFSE None	Cellpose	`CP_cyto2`	0.2178	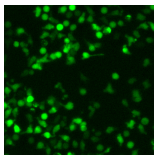
`lymphocytes_ricm`	RICM	Cellpose	None	0.2	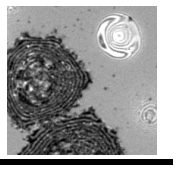

Table S5 Event detection models. We trained the following 1D DL models to classify and regress events of interest. The mean event response, centered at the event time is shown for each channel in the pattern column.

Name	Signals	Task	Pattern
lysis_H_PI	Hoechst PI	Strong PI intake	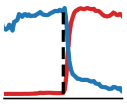
lysis_PI_area	PI area	Strong PI intake	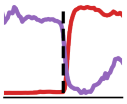
NucCond	area	Nucleus shrinking	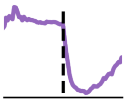

Supplementary Figures

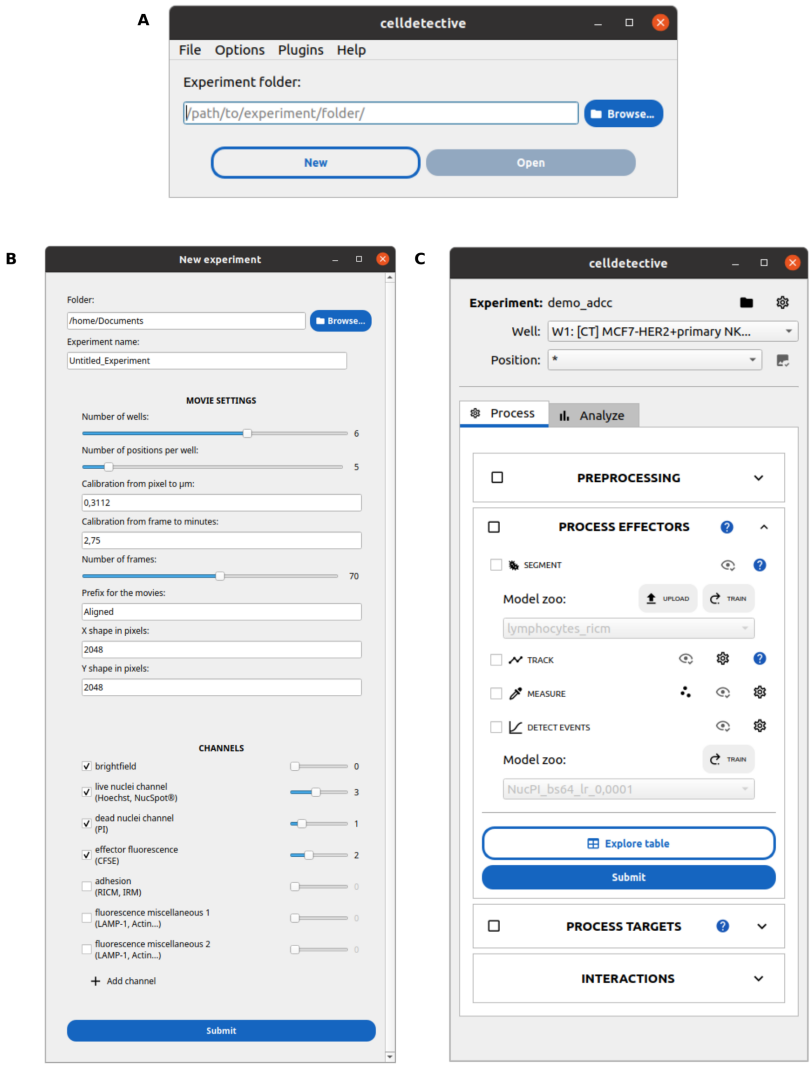

Fig. S6 Main GUI windows: A) Experiment project selection window. B) GUI to generate a new experiment, where the user provides the metadata. C) Main interface after loading a project. The process block for the effector population is unravelled, showing the 4 main steps detailed in Fig. 1.

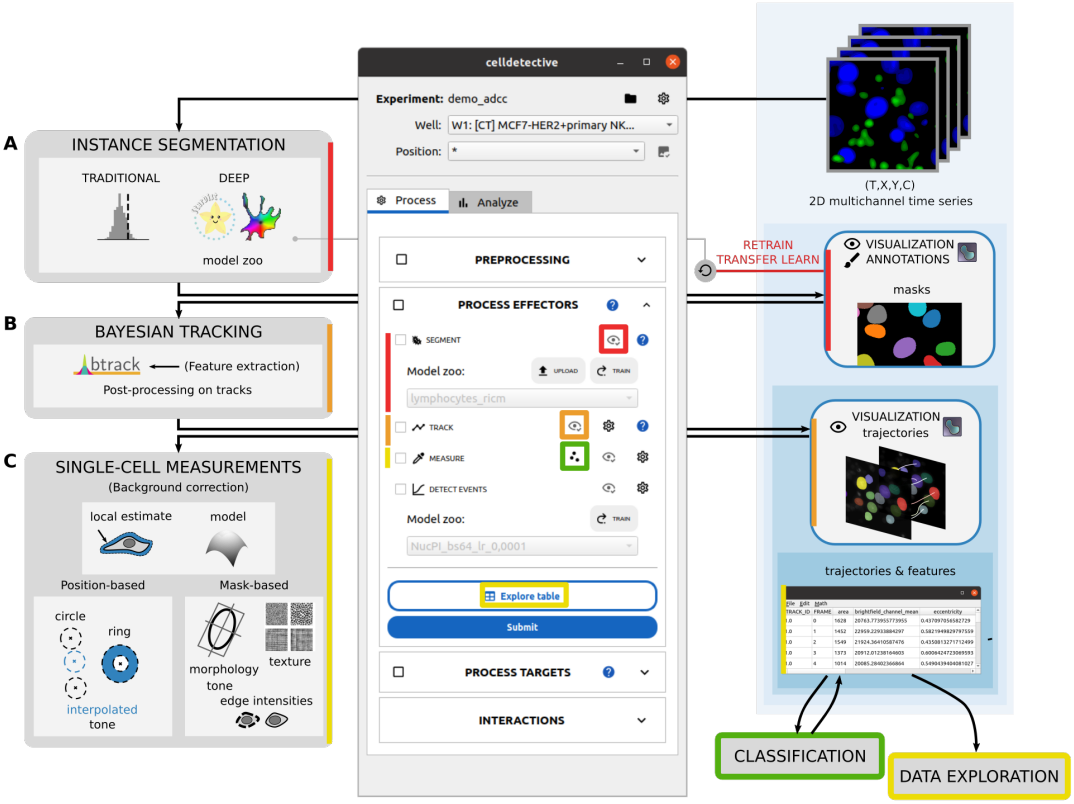

Fig. S7 Processing modules to extract single cells: Processing modules are shown on the left, with brief illustrations of the main options, while the output and visualization modules are represented on the right side, following Celldetective's graphical structure. A typical pipeline features successively (from top to bottom): A) an instance segmentation (either with traditional thresholding method or a Deep Learning model, stored in a model zoo, using StarDist [35] or Cellpose [37]). The output data are masks, which can be visualized and annotated using napari [56], for correction or model retraining. B) Bayesian tracking associated with feature extraction (btrack [41]), the output data being trajectories, which can also be visualized with napari. C) Single cell measurements of intensity, morphology, texture (based on cell position or on mask), the output being tables of trajectories enriched with features.

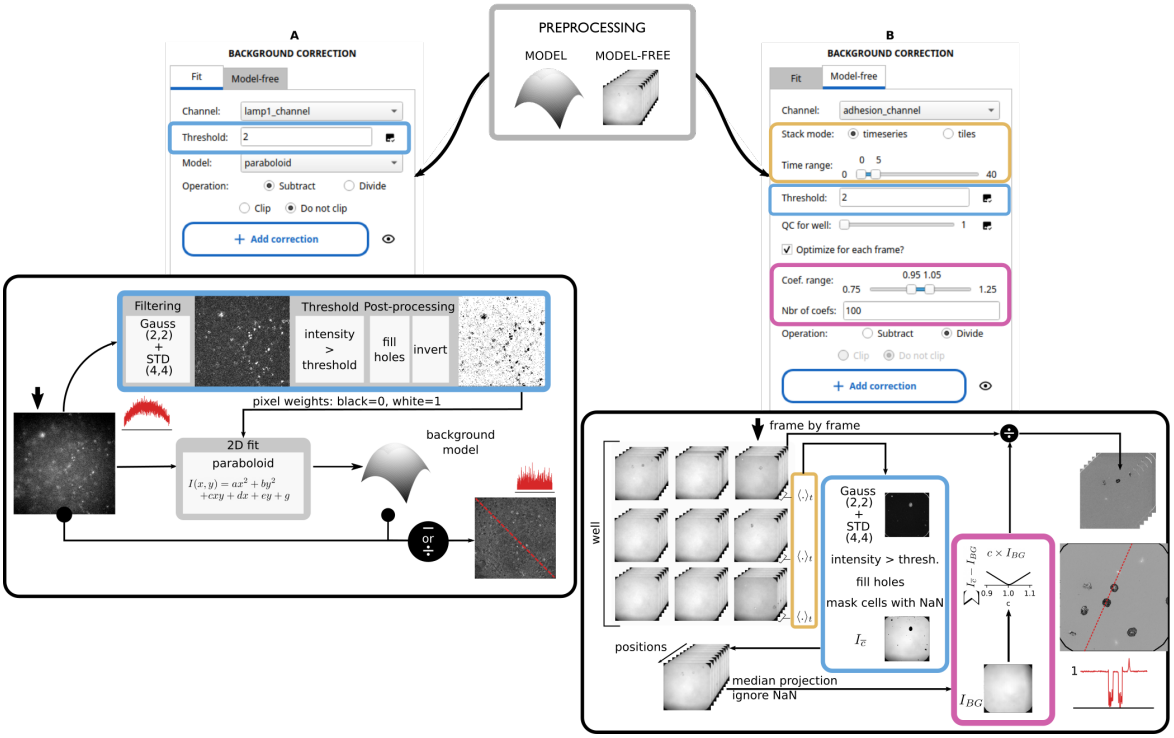

Fig. S8 Background correction methods. Screenshots of the background correction tabs in the software and illustration of the associated pipeline. Colored bounding boxes match graphical parameters to their role in the pipeline. The thick black arrows indicate the starting point of the pipelines. A) The steps for a fit-based correction involve selecting a channel of interest, setting a threshold on the standard-deviation filtered image to exclude the cells (done graphically with a viewer). Then a model (either plane or paraboloid) is fit on the background pixels for each image. The fitted background is either subtracted or divided, with or without clipping. B) With the model-free approach, a single background is reconstructed per well, following the same threshold approach but leveraging the multi-positional information to construct a median background. Instead of applying the background directly, it is amplified to minimize the difference with the current image's background. As with A), the background is then either subtracted or divided, with or without clipping.

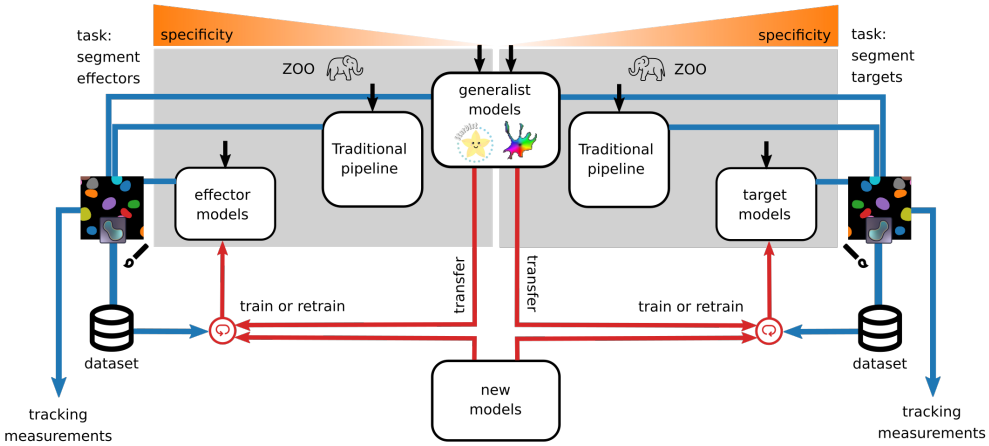

Fig. S9 Overview of segmentation strategies. The principle is illustrated for a mixture of two cell populations, effector and targets. Celldetective provides several entry points (black arrows) to perform segmentation, with the intent of segmenting specifically a cell population (left: effectors, right: targets). The generalist DL models are listed in Tab. S2. Specific DL models are listed in Tab. S3 for targets and Tab. S4 for effectors. The traditional pipeline refers to a thresholding method accessible through the GUI (see Fig. S11) and which can serve as a starting point to prepare a dataset for training a new DL model. The masks output from each segmentation technique can be visualized and manually corrected in napari. Exporting those corrections into a dataset of paired image/masks can be used either to fit a generalist model (transfer learning) or train a new model from scratch.

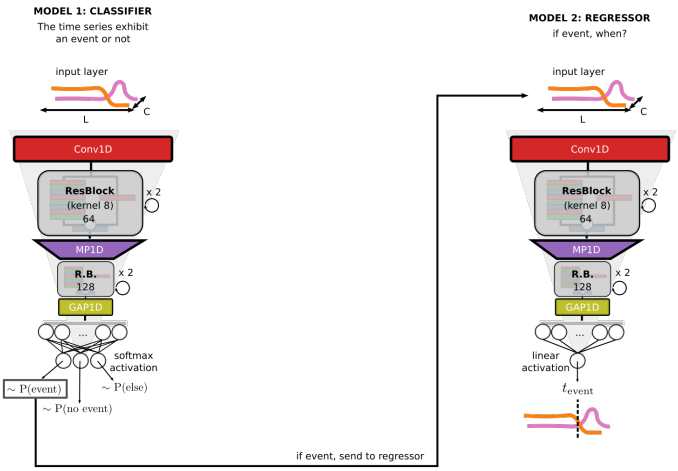

Fig. S10 Event detection model architectures. The event detection models consist of two CNN-based models called back to back during inference to 1) classify single-cell time series and 2) detect the event times from the same time series. The models share a similar architecture of a first 1D convolution, followed by ResBlocks encoding the time series into either three neurons with a softmax activation for the classification problem (three classes) or one neuron with a linear activation for the regression problem. As illustrated here, only the time series that were classified as "event" are sent to the regressor model.

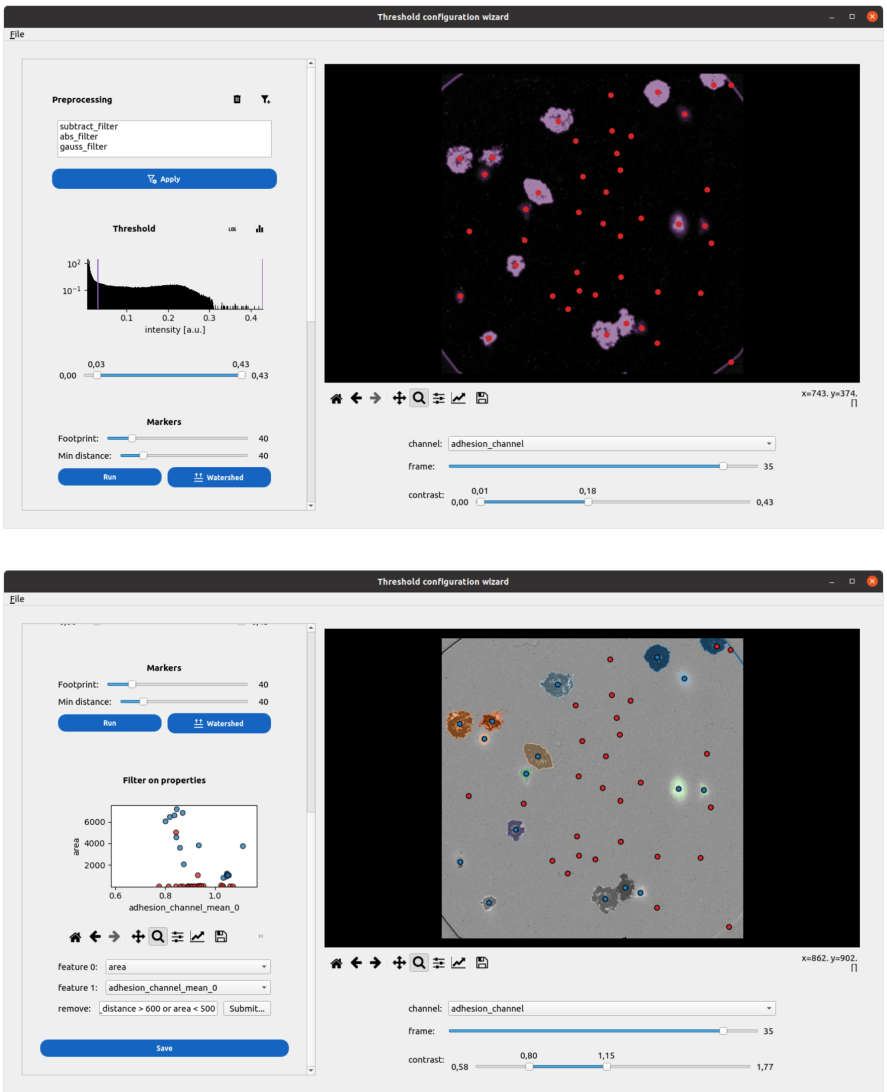

Fig. S11 Designing a traditional segmentation pipeline. Screenshots of the traditional segmentation pipeline configuration interface applied to a normalized RICM image of spreading primary NK cells. Top: User-selected mathematical operations (subtraction, absolute value) and preprocessing filters (Gaussian blur) are applied to the image, with results displayed in real-time on the right. A binary mask, set using an interactive thresholding slider, is overlaid on the transformed image in purple. Spot detection is then performed on the Euclidean Distance Transform of the binary mask, using parameters for footprint size and minimum object distance; detected spots are shown as red scatter points. Bottom: After applying the watershed algorithm, the instance segmentation of cells is overlaid on the original normalized RICM image. The user can set filters on object features to exclude false positives; rejected cells are marked in red in both the feature scatter plot and the image.

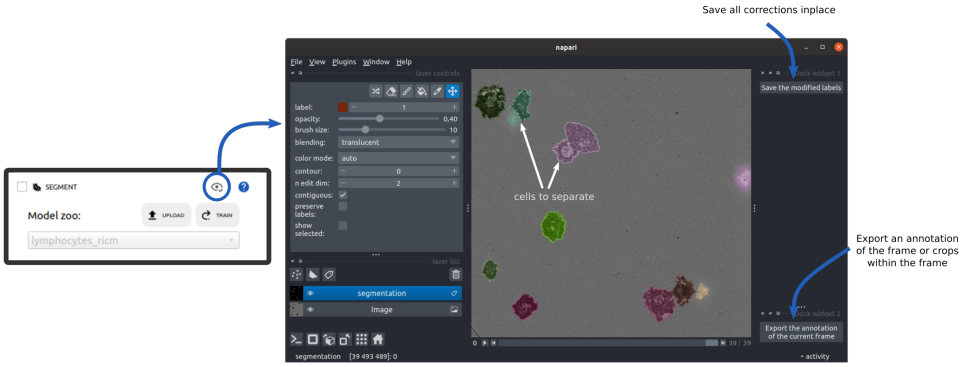

Fig. S12 Segmentation correction and annotation. To view segmentation results, the user can click the "eye" button in the segmentation module, which opens images and labels in napari. Shown is a screenshot of a segmentation outcome for a normalized RICM image of spreading primary NK cells, with labels overlaid on the image. The user can correct the masks directly on the image, for example, to separate cells indicated by white arrows. New labels can be assigned and saved, and the full set of corrected masks can either be saved in place (top-right plugin) or exported as a training sample for a segmentation model (bottom-right plugin).

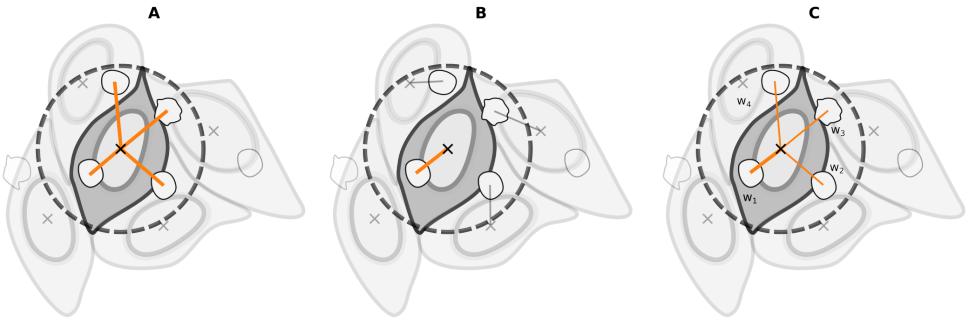

Fig. S13 Neighbor counting methods: A) All neighboring cells in contact or within the isotropic neighborhood are linked to the reference cell (inclusive method). B) Each neighboring cell is linked exclusively to the closest reference cell (exclusive method). C) Neighboring cells in contact or within the isotropic neighborhood are linked to the reference cell, with weights inversely proportional to their number of neighbors.

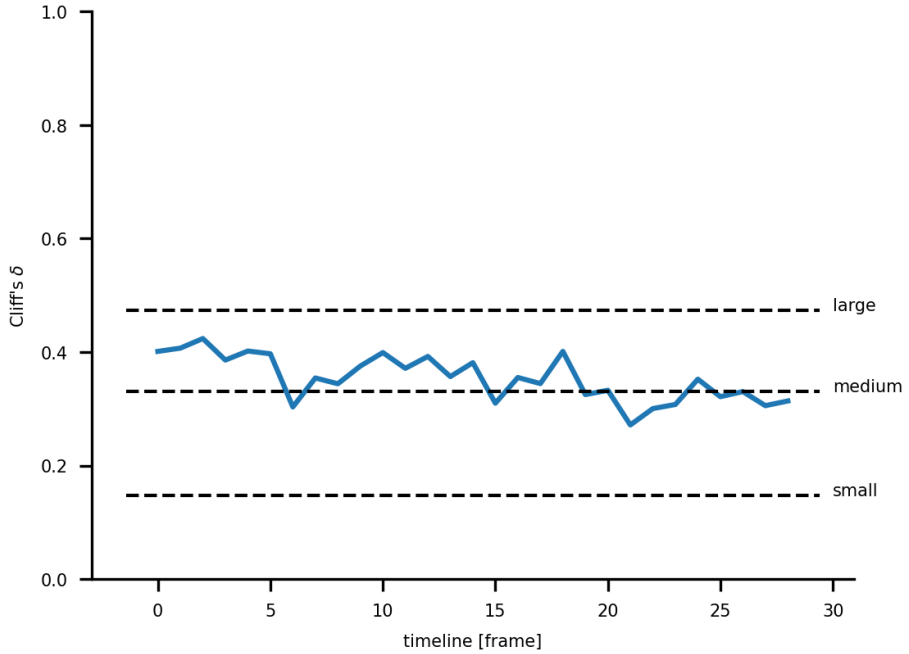

Fig. S14 Effect size at each time point: Cliff's Delta between the simulated sum of two distributions (CE4-21/off-contact/HER2+ + CE4-X/in-contact/HER2+) and CE4-21/in-contact/HER2+ computed at each timepoint, independently.